ISTITUTO ITALIANO DI TECNOLOGIA

Dibris

UNIVERSITÀ DEGLI STUDI DI GENOVA

Doctoral Thesis in Bionanotechnologies

Cell membrane interactions with 3D multifunctional nanostructures

Candidate: Valeria Caprettini

Supervisor: Francesco De Angelis

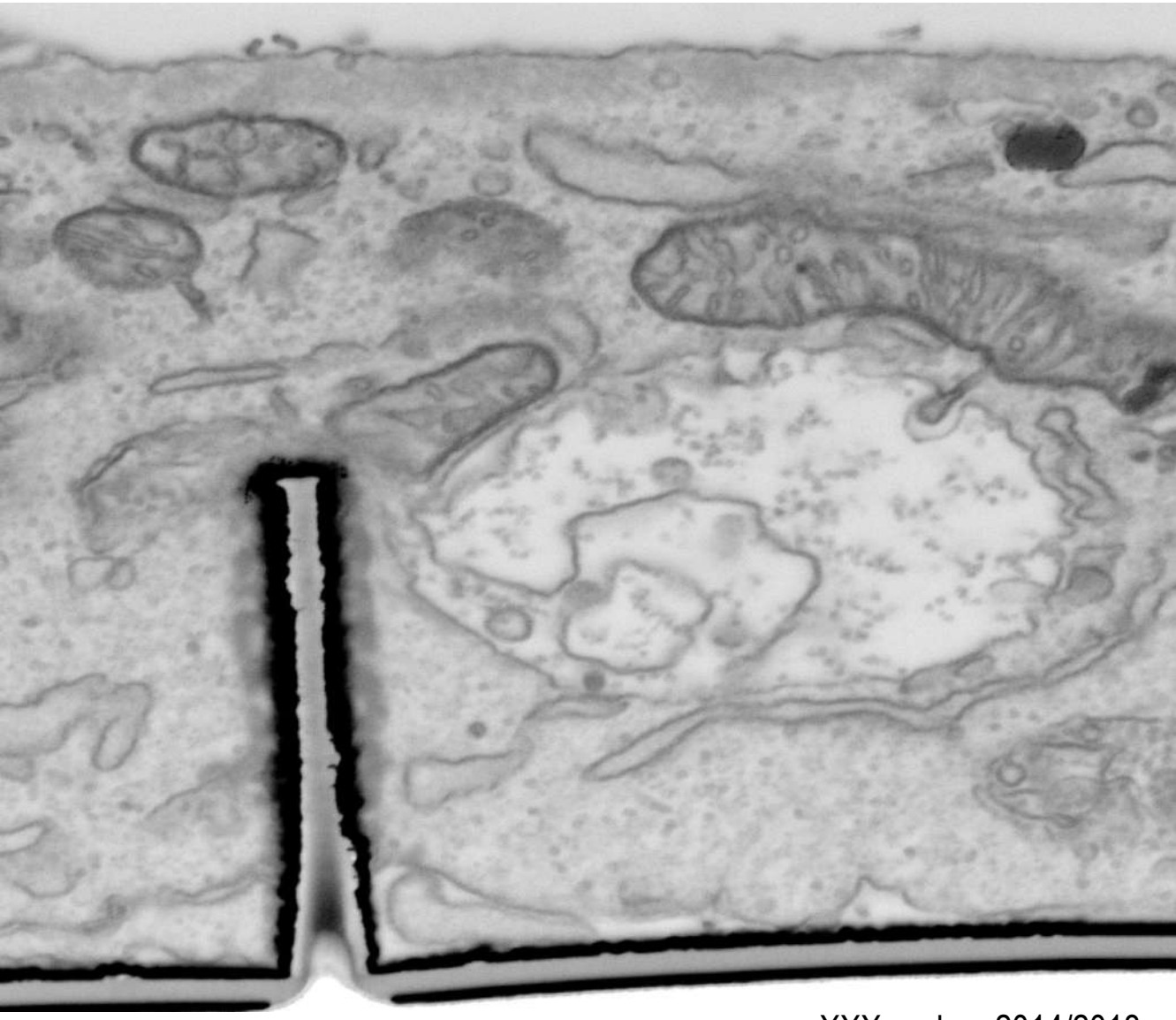

XXX cycle – 2014/2018

Contents

Abstract

In recent years, cells studies are often carried out with the help of three-dimensional (3D) nanostructured substrates. These kind of substrates can be useful in assisting the access in to the intracellular compartment and the delivery of molecules through holes or nanochannels, as well as in increasing the contact area of a cell with an electrode during electrical recordings. At the same time, little is known about the interaction of the cells with these substrates and their dynamics on them, and even less it is known about the effects of the electroporation on the cellular membrane. Surface Enhanced Raman Spectroscopy (SERS) is a powerful and helpful technique in this regard being label-free and not invasive.

This thesis explores the universe of the interface within 3D nanostructured substrates and cultured cells in different ways. First, it develops a 3D nanofluidic platform able to interface with living in vitro cells and locally electroporate them, intracellularly injecting molecules. Subsequently, the interface between the 3D nanostructures and the cultured cells is investigated by electron microscopy together with ionic milling, revealing a tight sealing between the substrate and the plasma membrane. Finally, a plasmonic 3D substrate is exploited to study the cell membrane dynamics on it in presence of an *in situ* electroporating pulse train. The findings of the present work are promising to unveil the mechanisms of the plasma membrane reforming after electroporation.

Chapter 1

Introduction

The cell is the building block to life as we know it, being the single unit of plants, animals and humans. There are two different kinds of cells, prokaryotic and eukaryotic. Both of them are composed by an external membrane that separates the organism and all its content from the environment, and that arranges the interactions with the surroundings. Nutrients go through this plasma membrane as well as molecules that drive the interactions with other cells and tissues. The cell membrane is composed by a lipid bilayer in a liquid state with proteins embedded and protruding towards the inside - the cytoplasm -, the outside, or across the whole membrane (*trans-membrane* proteins). The liquid phase is due to the unsaturated hydrocarbon tails of the fatty acids and cholesterols that mainly compose the plasma membrane [1], [2]; this conformation allows proteins and lipids to move in the plasma membrane. In the last decades, different domains of the plasma membrane have been identified as "lipid rafts" [1]. Lipid rafts are tightly packed domains of the lipid bilayer, formed by a majority of sphingolipids and phospholipids with saturated hydrocarbon chains that resolves in a denser, ordered area of the plasma membrane [3]. The exact role of the lipid raft is still under investigation but there are strong evidences that these rich proteins domains are related to the

cell bioactivity [4].

There are different mechanisms for molecules to go in and out the cells; small particles like oxygen can diffuse through the membrane, while nutrients and ions are actively carried in through specific protein channels and some products of the cell metabolism are carried out. The plasma membrane also has an important and active role in the trafficking of molecules; in fact, it can engulf molecules and particles creating vesicles that are incorporated in the cytoplasm in a process called *endocytosis*, or vesicles inside the cytoplasm can merge within the plasma membrane releasing molecules outside the cell, and this process is called *exocytosis*. Recent studies suggest that exocytosis processes also play a role in the membrane repair after a traumatic event [5].

The *trans-* and *cis-* membrane proteins are responsible for some of the intra and extracellular trafficking mechanisms, for the signaling reception, for the bending of the membrane and the subsequent endocytosis or exocytosis, for the movement of the cell and more in general for its interaction with the environment [6]. Evolution has shaped the plasma membrane to be flexible and resistant to preserve the cell from external agent attacks and to maintain its healthiness.

In order to study the cell response to external stimuli, to test new drugs for treating diseases or to record the electrical activity of neuronal networks to understand neuronal pathways, the plasma membrane acts as an obstacle that needs to be overcome [7]. Over the years, biology and medicine exploited technology and its development in the nano-scaled world to tackle the problem of gaining the access to the intracellular space with several different techniques. Some methods provide for modifications in the chemical structure of molecules to promote their natural uptake from the cells by endocytosis pathways. More complex biochemical techniques involve the encapsulation of the desired molecules in vesicles or in virus-like nanoparticles and the subsequent coating of these carries with particles that can be recognized by receptors on the cell

membrane and therefore uptaken [8].

Physical or mechanical methods relate to the ability of creating transient hydrophilic nanopores in the lipid bilayer, allowing molecules to diffuse from the extracellular environment to the cytoplasm. These mechanical methods have been implemented with nanofabricated surfaces to create the nanopores through for instance laser-assisted and plasmonic poration [9], [10], microinjection [11], [12], acoustic poration [13] and electroporation [14], [15].

1.1 Electroporation and delivery

One of the most common techniques explored to gain the intracellular access is *electroporation* and it exploits an electrical pulse train applied for a limited time on a cell culture. If the effective *trans-membrane* voltage is high enough ($\sim 1V$), the lipid bilayer temporary rearranges its molecular structure increasing the permeability of the plasma membrane, thus allowing the access to the intracellular compartment through hydrophilic nanopores [16]. The dimensions of the nanopores created by electroporation have been largely studied together with their persistency in time, showing an average resealing time in the range of few minutes [17], [18], [19]. If the radius of the nanopores becomes too large or when too many nanopores are opened, the plasma membrane is no longer able to heal and the situation often resolves in the cell death [20].

This method has been originally developed by applying very high voltages on cells in suspension between two flat electrodes [21]. Hereafter, with the development of nanotechnologies the technique has been refined and poration has been performed also on adherent cells through 3D nanostructured surfaces and microfluidic devices [22], [23].

The applications of electroporation to adherent cells are manifold such as the recording of intracellular activity of cardiomyocytes [14] and neurons [24], the delivery of molecules and genetic material inside the porated cells [25],

[10], or the sampling of the intracellular content of the targeted cells [26]. However, even if 3D nanostructured surfaces demonstrate themselves of being suitable platforms to electrically porate the lipid bilayer, applying an electrical field in aqueous solution can create reactive oxygen species (ROS) from the dissociation of water molecules [27]. The minimum applied voltage on the single water molecule to create hydrolysis at standard conditions (25 ℃) is in fact 1.23V [28], [29], which is a low value compared to the voltage applied over the whole samples in nanostructured devices used to perform electroporation [30]. ROS are potentially toxic for the cellular cultures, provoking DNA and RNA mutations, starting processes of apoptosis and creating oxidative stress to the mitochondria and the cell culture [6], [31]. Theoretical studies have already explored the *trans-mmebrane* voltage needed to open nanopores on cellular membranes; according to the simulations, only 1V is required to porate the membrane [32]. However, to have that kind of effective *trans-membrane* voltage, the applied voltage on the whole system needs to be much higher depending on the distance of the electrodes from the lipid bilayer. In fact, considering two flat electrodes far away from each other, the voltage follows a trend of $1/r$ meaning that the farther the cell culture from the electrodes, the lower the net *trans-membrane* voltage. Changing the geometry of the electrodes also changes the $V(r)$ distribution, leading nonetheless to decay in space when away from the electrodes.

Growing the cells directly in adhesion with one of the electrodes reduces drastically the applied voltage needed to open transient nanopores in the cell membrane, getting as low as the minimum voltage required [14]. The nanopores are created only in close contact with the nanoelectrodes, because the plasma membrane adherent to the electrode is the only portion that feels a sufficiently high *trans-membrane* potential. This very interesting feature that finds great applications in the intracellular recording of electroactive cells, has some drawbacks when it comes to applications in the delivery of particles; in

fact, molecules dispersed in the cell bath are not able to diffuse in to the cytoplasm because of the tight sealing of the cell membrane with the substrate, and since now it was not possible to electrically porate cells to perform delivery with very low voltages.

1.2 Tight sealing between cells and 3D nanostructured surfaces

In recent years, a lot of studies have been done on the interface between biological samples and nanostructured substrates mainly for the importance of their interactions in the development of bioelectronics devices [33], medical implants [34] and in the emerging field of regenerative medicine [35], [36]. Rough and porous materials as well as 3D nanostructured surfaces are vastly used to couple with cells and tissues [37], [38], [39], but there still is a lack of knowledge in the adhesion and interaction of them.

To address these questions, optical microscopy in itself is not quiet useful because of the diffraction limit of the light, whereas fluorescence microscopy and super-resolution techniques are more suitable to approach the interface investigation [40]. However, fluorophores that binds with specific molecules have to be fed to the cells and the tissues, and experiments have to be carefully designed together with the optical setup to study how cells or tissues interact with the nanostructured materials [41], [42].

The acquisition times for the imaging in the super-resolution microscopies can be very long, as the data analysis that follows the experiments, and the experimental setup has to be finely re-tuned when changing each experiment. Overall, fluorescence microscopy and in particular super-resolution techniques are mighty but can be time consuming and require specialized figures to fix the setup and adjust it to the need of each analysis. A great advantage of fluorescence microscopy however, is the capability of investigate living *in vitro*

samples without the need to add fixatives such paraformaldehyde (PFA) or glutaraldehyde to the systems.

Being willing to abandon the investigation on living *in vitro* systems, electron microscopy is an alternative powerful approach that can make possible to visualize cell membrane, nucleus, organelles and DNA within the same sample preparation with no need to customize it for each experiment [43]. When the interesting portion of the samples is the interface with nanostructured substrates however, transmission electron microscopy (TEM) loses some of its capability. In fact, the sample need to be small enough to get inside the TEM (standard TEM grids are $3.05mm$ in diameter) and not too bulky (maximum $200nm$ thick), otherwise electrons are not able to go through it [44], [45]. It is possible to mechanically slice in advance the sample using a microtome, but in this way the nanostructured substrate could be ruined and also the mechanical blade could spoil the natural interface between the substrate and the biological sample when the cut is perpendicular to the substrate. Moreover, there is no *a priori* knowledge on where to cut the specimen, making the chances to guess the better area and expose the interested interface are thin. Scanning electron microscopy (SEM) together with focus ion beam (FIB) milling and polishing is a valid alternative, because of the fine control that can be reached over the dimension of the incision [46].

The preparation of the samples for electron microscopy (EM) involves several steps starting from fixing the biological specimen with a chemical glue (normally PFA or glutaraldehyde) that quickly kills the cells by crosslinking their proteins. The shape and the morphology of the sample are then preserved and maintained to be investigated. After fixing and staining the specimens, a last step is required in EM in which sample is either dried (for example by critical point drying technique, CPD), or plasticized in hexamethyldisilazane (HMDS) or in an epoxy resin [47], [48]. The CPD or the HMDS plasticization preserve very well all the external structures, but leave voids where the cells

contained liquid. On the contrary, epoxy resin infiltrates everywhere guaranteeing the filling of all the aqueous portion of the cell and allowing a very good contrast in the imaging. However, the epoxy resin process results in a bulk piece of crosslinked polymer. Using SEM to analyze these samples, CPD and HMDS plasticized specimens show a very well preserved surface features and the nanostructured areas can be easily spotted, but FIB milling reveals sponge-like sections of cells and tissues [49] (see Figure 1.1 a, b).

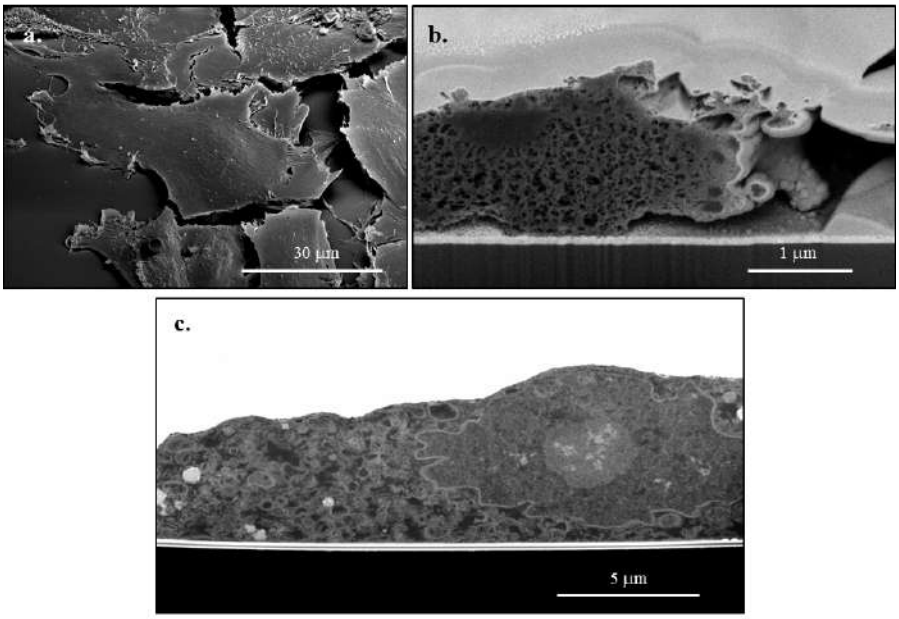

Figure 1.1: SEM images of fixed 3T3-NIH cells. a) CPD dried cell on tilted stage at 52°. b) FIB cross sectioned of a CPD dried 3T3-NIH cell. c) FIB cross section of resin infiltrated 3T3-NIH cell.

Resin-embedded samples by contrast allow a 40 nm resolution of intracellular organelles and membranes (see Figure 1.1), but the external morphology of the system (both cells and nanostructured substrate) is hidden in the thick

layer of resin, making impossible to localize *a priori* the area of interest [48].

Recent developments in the sample preparations made FIB/SEM cross section and imaging technique much more appealing to investigate the cell - material interface. In particular, a drain of the resin and a following wash with ethanol before its polymerization allows to remove the resin excess from the specimes [50], [51]. With this new preparation technique, the resin on the specimen that did not infiltrate inside the biological parts of the sample is washed away leaving the nanostructured surface exposed and visible to the microscope. The interesting area of the sample can be localized, milled and polished with the FIB while the SEM imaging reveals the cell membranes preserved and in contact with the different substrates.

1.3 Surface Enhanced Raman Spectroscopy on biological samples

There are many techniques for studying biological systems and one of the most spread is fluorescence microscopy. Nowadays, very high resolution have been reached even overcoming the light diffraction limits thanks to stratagems related to fluorophores, photoblinking and multi-photons approaches [41], [52], [53], [54], [55]. However, using fluorophores, dyes or fluorescent proteins to investigate cells and tissues systems can have drawbacks, mainly due to the influence of these molecules to the intracellular processes and the system behaviors [56]. Moreover, only labelled molecules can be detected simultaneously, thus limiting the variety of information that can be collected during a single experiment.

Raman spectroscopy on the contrary, is a technique that allows the simultaneous detection of multiple molecules; in addition it is label-free, meaning that it is less invasive in respect to fluorescence microscopy since the system does not need to be stained before performing the experiments [57], [58].

Raman spectroscopy is based on the detection of the vibrational and rotational modes of the molecules that interact with a monochromatic source in an inelastic way. Each molecule has its own vibrational modes that represent its fingerprints when excited with a laser source; by studying the spectrum of a substance it is possible to identify the molecules that are contained in it. A way to exploit Raman spectroscopy in complexes systems like *in vitro* cells is Raman imaging, in which for each pixel a Raman spectrum is collected in a submicron excitation volume [59]. The typical Raman cross section per molecule however, is between 10^{-30} and $10^{-25}\,cm^2$, while the fluorescence cross section is roughly ten to fifteen times higher ($10^{-16}\,cm^2$) [60], [61]. Being the inelastic light scattering a very weak phenomenon, Raman spectroscopy requires high acquisition times and the auto-fluorescence emissions are often more intense, covering the signals of interest [62].

Nanotechnology comes into aid with the plasmonic features of particular nanostructured materials. Plasmons are collective oscillation of the electronic cloud (the free electron density) in a metallic material. Localized surface plasmon resonances (LSPR) are collective electron charge oscillations at the metal-dielectric interface that are excited by light. At their resonant wavelength $\lambda_p = 2\pi c/\omega_p$ they show highly localized enhanced near-field amplitude in metallic nanostructured geometries that quickly decays away from the nanostructures surface. To generate LSPR, the real part of the relative permittivity (ϵ_r) of one of the materials has to be positive (a dielectric), while the real part of the relative permittivity of the other material needs to be negative (normally a metal or a doped semiconductor) and larger in respect to that of the dielectric.

By shaping the geometry of the nanostructures, it is possible to make them resonant at specific optical frequencies and to generate hot-spots of highly enhanced field in extremely localized regions [63]; these substrate are used in the Surface Enhanced Raman Spectroscopy (SERS) to enhance the Raman

signal of molecules adsorbed on or in very close proximity to the hot-spots.

SERS reveals itself to be a suitable compromise for the study of biological systems [64] being able to enhance the Raman signal up to 14 or 15 orders of magnitude [60], [65]. In recent studies, 3D plasmonic nanostructures have been used to investigate the Raman spectra of living cultured cells [62], [66]. The 3D nanostructures have the capability to locally enhance the electric field and consequently the Raman signal coming from the cells that are tightly sealed around them; the largest enhancement is concentrated in the hot-spot located at the tip of the 3D nanostructure. The SERS substrate can be engineered to be resonant at a chosen wavelength, allowing for example to exploit a $\lambda = 785\,nm$ laser source for Raman spectroscopy; this wavelength is particularly suitable to study biological samples because photons in the near-IR range have an insufficient energy to excite the majority of the fluorescent phenomena within cells and tissues, and provokes much less phototoxicity in respect to light in the UV or in the visible range [57].

1.4 Aim of the work

The present thesis aims at exploiting a 3D nanostructured surface that can interact with *in vitro* cultured cells for multiple purposes such as electrical poration and intracellular delivery of molecules. Additionally, taking advantages of the 3D nanostructures plasmonic properties, it is presented a SERS study on the permeabilization of the cell membrane by electrical pulse application (electroporation) and its subsequent rearrangement.

The device is composed by patterns of 3D hollow gold nanoelectrodes on which cells are cultivated. The close proximity of the cell membrane to the nanoelectrodes allows generating a high *trans-membrane* potential exploiting a low applied voltage thus limiting the formation of ROS within the cell culture. In this way, a *soft-electroporation* is performed and nanopores in the

plasma membrane are opened in correspondence of the 3D nanoelectrode tips. Since the vertical nanoelectrodes are hollow, molecules can flow through the inner nanochannel from a separated compartment beneath the culture well and diffuse inside the porated cells.

To better understand the sealing of the plasma membrane around the 3D nanoelectrodes, FIB slicing and SEM imaging are performed on the device. The membrane results always in close contact with the three-dimensional nanostructures, tightly wrapping the vertical nanoelectrode.

Tuning the dimensions in height and diameter of the gold 3D nanoelectrodes it is possible to couple laser light with these nanostructures and exploit their plasmonic proprieties to locally enhance the Raman signal of the molecules in contact with them.

In the last part of the present work, this ability has been used to study the plasma membrane dynamics of *in vitro* living cells cultured on the 3D plasmonic substrate. The device geometry has been revisited to be plasmonic at the desired wavelength and removing the nanofluidic proprieties; a new substrate has been designed to address pattern of 3D nanoelectrodes individually within the same device. The dynamics behaviors of the plasma membrane have been monitored by means of SERS over 30 consecutive minutes and electroporation have been induced during the experiments.

This study aims at enriching the knowledge about the nanopores creation in the cell membrane after the application of an electroporating train pulse, and the rearrangement that follows this permeabilization. Results have been compared to the same analysis of the unperturbed system and with the data already present in literature finding great agreement.

Chapter 2

Materials and Methods

2.1 Fabrication

The 3D nanostructures are fabricated on thin Si_3N_4 membranes ($100\,nm$ or $500\,nm$ thick) or on quartz Multi Electrode Arrays (MEAs) depending on the design of each specific set of experiments. In particular, delivery experiments were performed on devices fabricated on Si_3N_4 membranes so to have 3D hollow nanostructures protruding on one side of the device, being the back of the membrane accessible through the inner channel of the 3D nanostructures. Raman Enhanced measurements have been performed on MEA devices, in which the 3D nanoelectrodes have been fabricated on the flat electrodes of a custom made quartz chip.

The fabrication process of the 3D nanostructures includes the inversion of an optical polymer ($S1813$ by Shipley) by the secondary electrons emitted during focused ion beam (FIB) milling; this process was recently developed and published [67]. In detail, a thin silicon nitride membrane (Si_3N_4) on a bulky silicon substrate is immersed in acetone and isopropanol to be cleaned and then dried by gently blowing N_2 on it. The resist $S1813$ is spin-coated at $4000\,rpm$ to a final height of $1.8\mu m$. The back of the Si_3N_4 membrane is

coated with some tenth of nm of gold to prevent charging during the milling process and then gallium ions are focused on the back of the Si_3N_4 membrane - or from the top of the quartz MEA device through a sacrificial layer of gold - in regular patterns with defined pitch. The secondary electrons generated when the beam interacts with the resist invert the surrounding polymer making it insoluble; in this way, the resist will not dissolve when immersed in a solvent (acetone) that will remove instead the unexposed polymer. By tuning the current of the beam, the milling depth and the height of the resist the 3D nanostructures can be fabricated with a variety of sizes in diameter and height. The 3D nanostructures are then sputtered in gold to make them electrically conductive, plasmonically active and biocompatible.

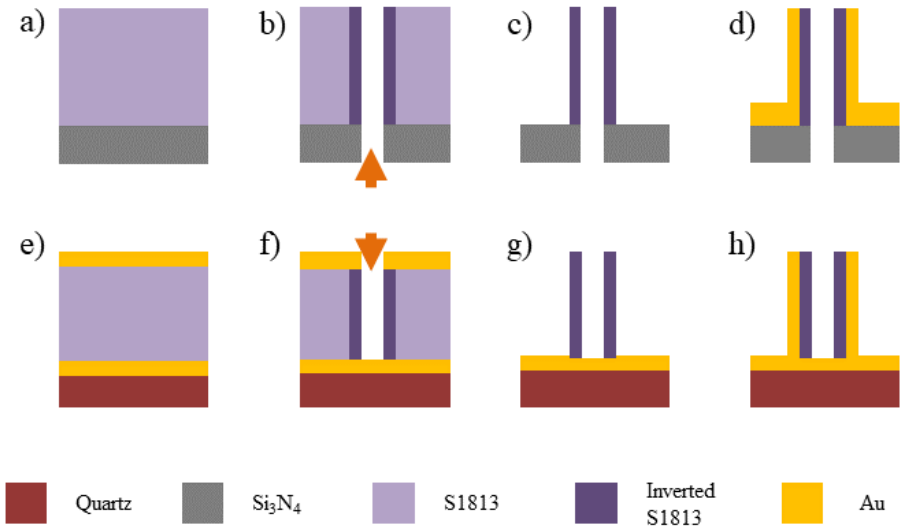

Figure 2.1: Fabrication process of 3D nanoelectrodes. a) - d) Fabrication process on thin Si_3N_4 membrane. The FIB milling occurs from the bottom of the device. e) - h) Fabrication process on a quartz MEA. In this case the FIB milling occurs from a top sacrificial layer of gold that is wet-etched before the removal of the unexposed resist.

In the present work, the height of the 3D nanostructures has been kept constant at $1.8\mu m$ and two different diameters have been used, namely $500\,nm$ of external diameter in the *soft-electroporation* experiments and $100\,nm$ in the Raman enhanced experiments. The fabrication process is schematically represented in figure 2.1.

The final devices are either a single electrode patterned with different arrays of large ($500\,nm$ in diameter) 3D hollow nanoelectrodes [10], or a MEA-like device with 24 flat small electrodes, each patterned with a single array of thin ($100\,nm$ in diameter) 3D plasmonic nanelectrodes [68]. Figure 2.2 a, b shows the MEA device with a magnification at the optical microscope of six flat electrodes; on each flat electrode, arrays of 3D nanoelectrodes are fabricated. SEM image of a three-dimensional nanoelectrode and its cross section are in figure 2.2 c, d.

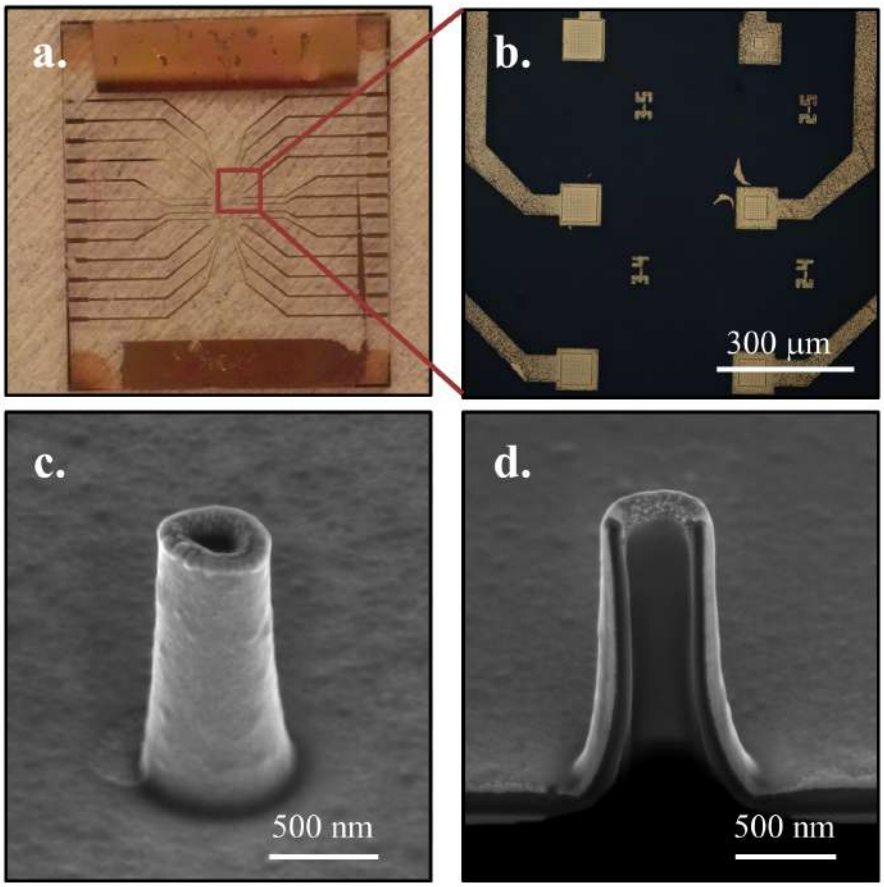

Figure 2.2: a) Picture of a custom-made MEA with b) magnification of six flat electrodes. Each of the flat nanoelectrodes have arrays of 3D nanostructures fabricated on them. c) SEM image of a 3D hollow nanoelectrode used for electroporation and delivery of molecules and d) SEM image of its FIB cross section, where the inner nanochannel is clearly visible.

2.2 Passivation

In both the configurations, either single electrode or multiple electrodes, a passivation step has been implemented to generate electroporation only through the tip of the 3D nanostructures and not from irregularities on the planar gold surface.

The passivation step required optimization and multiple approaches have been explored. The first attempt was made with a spin-coated layer of PMMA on the nanofabricated surface. PMMA is a well-known biocompatible polymer [69], [70] that can have different densities resulting in various thicknesses due to the changing in the surface tension during the spinning. The final device should have at least $1\mu m$ of passivation layer, so to insulate the flat surface covered in gold from the cell culture and to leave exposed a suitable portion of the 3D nanostructures. The process needs to be as easy as possible and reproducible over the whole sample and on different samples. Several densities of polymer 950 PMMA have been tested with different spinning rates but the results were never satisfying. The process was seldom reproducible even bringing uniformity problems, showing a different interaction with the 3D nanoelectrodes also on the same device (see figure 2.3 a, b). Some dilutions where too dense and the entire 3D nanoelectrodes were covered by it, while other dilutions resulted in a too thin flat polymer layer (figure 2.3 c, d, respectively).

A second attempt for creating the passivation layer involved the evaporation of a silicon oxide (SiO_x) layer on the device. Since the evaporation process deposits the material vertically, the result would have left the side walls of the 3D nanoelectrodes free from the silicon oxide coating, while the flat substrate would have been covered by a glass insulating layer. However, the thermal evaporator used to deposit this passivation layer did not allowed control over the purity of the deposited material and the resulting SiO_x revealed itself to be toxic for the cell culture.

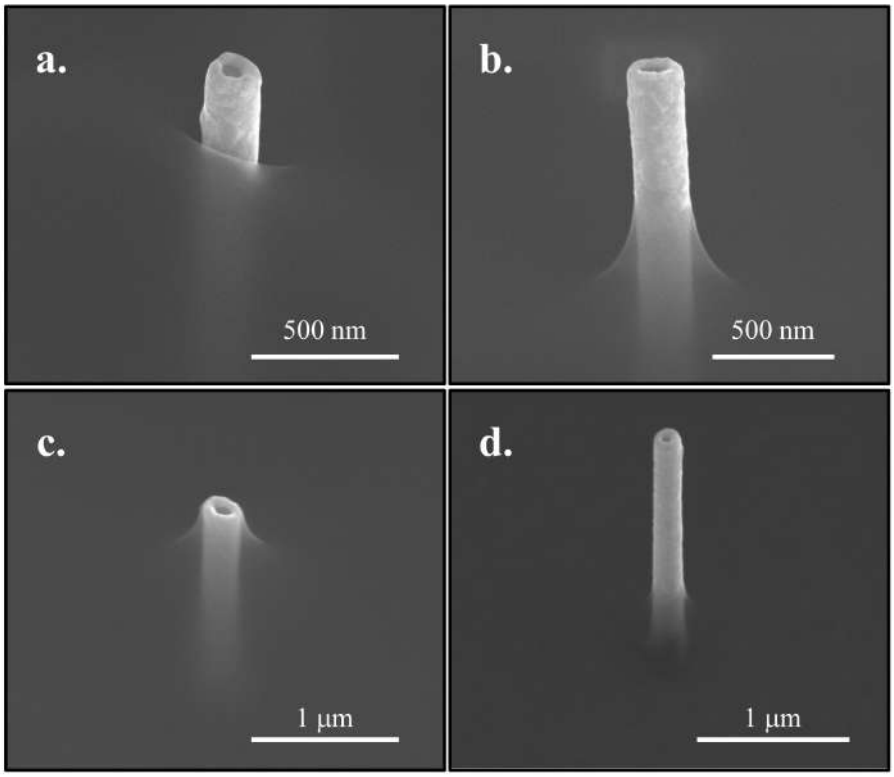

Figure 2.3: Passivation tentative with 950 PMMA. a), b) SEM images of 3D nanoelectrodes within the same device spin-coated with 950 PMMA A8 at 4000 rpm. The meniscus is different from 3D nanoelectrode to 3D nanoelectrode, and the amount of exposed tip is not the same. c), d) SEM images of different dilution of PMMA that resulted in either a too thick passivation layer, or a too thin one.

Pursuing the possibility of using glass to insulate the flat part of the device, an Atomic Layer Deposition (ALD) process was tested. This deposition technique allows for a much more pure deposited material in respect to the one thermally evaporated, but the deposition is homogeneous over the entire sample instead of vertical as the previous one. In fact, ALD processes consist in the sequential exposure of the desired surface to different gaseous species (the precursors); each of the gaseous specie interacts with the surface of the material until all the possible sites of binding are saturated and a single layer is deposited. At that point, the chamber of the ALD is cleaned and the following precursors are pulsed inside the chamber to create a second layer on the surface with a new ALD cycle. In the end the substrate presents itself entirely covered in pure material (in the present case SiO_2), and there is the need of removing the passivation from the lateral walls of the 3D nanoelectrodes leaving the silicon dioxide on the flat substrate. Hydrofluoric acid (an aqueous solution made by hydrogen fluoride, HF) is the best candidate to etch the SiO_2 from the 3D nanoelectrodes, being its ability to dissolve glass known since the seventeenth century [71].

A polymeric mask of PMMA has been spin-coated on top of the glass covered substrate, exploiting the information already gathered on the different height of the PMMA depending on the velocity of the spinner and on the density of the polymer. Hydrofluoric acid in fact, should etch the PMMA polymer with a very slow rate compared to the rate of dissolving the silicon oxide on the vertical walls of the 3D nanoelectrodes. A wet etching procedure in hydrofluoric acid is then developed to remove the SiO_2 from the lateral walls of the 3D nanoelectrodes followed by the removal of the mask layer of PMMA. SEM imaging is performed to assess the validity of the method (see figures 2.4 a, b, c) but again the results were not satisfying. PMMA mask resulted not so effective as should have be, allowing the penetration of the acid in proximity of the 3D nanoelectrodes and from the edge of the device. In that way, the

silicon oxide is etched also in proximity of the 3D nanoelectrodes at its base exposing part of the gold on the flat substrate (see figure 2.4 d, e).

In the end, the best choice to passivate the device resulted to be a layer of an epoxy polymer (SU8) spin-coated on the device to a height that matches the one of the 3D nanoelectrodes and cross linked by the exposure to UV light. Part of the device is masked from the UV lights and the unexposed resist is then developed in SU8 developer so to leave a portion of the sample electrically accessible; in particular, an angle of the square samples used in the delivery experiments, and the final part of the conductive traces in the MEA-like devices. Afterwards, a plasma etching procedure has been implemented so to leave only $700\,nm$ of the 3D nanostructures free from the SU8 polymer and electrically conductive (see sketch in figure 2.5). Hard bake is performed to make the polymer inert and to ensure the complete evaporation of the solvents, making the flat substrate biocompatible [15]. This choice was dictated not only by the reproducibility of the process but also by the easiness of the protocol.

The final 3D nanostructures, both the small and the large in diameter, show only a gold tip to the surroundings, being the flat substrate passivated by the inert SU8 epoxy polymer; SEM images of the single nanoelectrodes with the respective cross section are shown in figure 2.6.

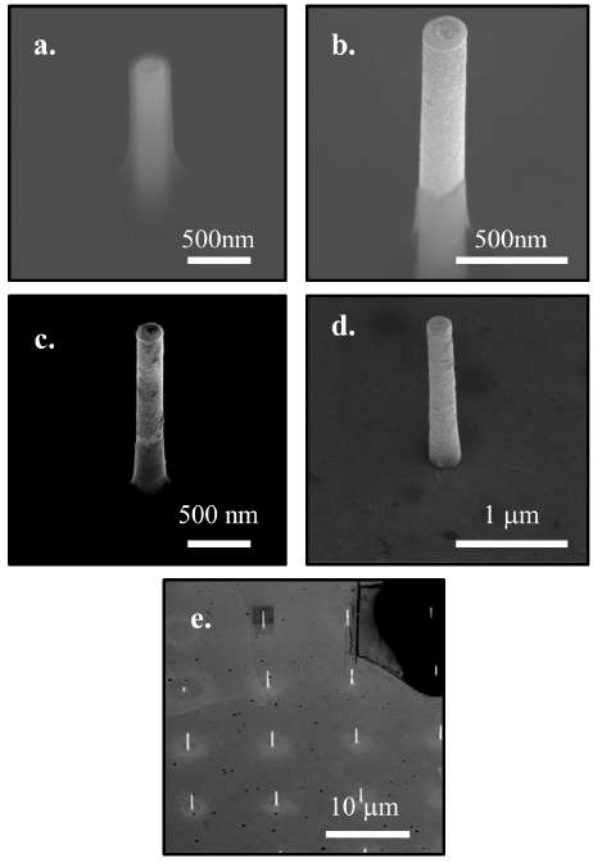

Figure 2.4: SEM images of the passivation trial with ALD deposited SiO_2 and removal with hydrofluoric acid of the glass from the vertical walls of the 3D nanoelectrodes. a) SEM image of a 3D nanoelectrode with $70\,nm$ of SiO_2 heterogeneously deposited on the device and a mask layer of PMMA spin-coated on the device. From the SEM image is not possible to distinguish the SiO_2 from the PMMA. b) SEM image of the 3D nanoelectrode exposed tip after 3 minutes of wet etching with 4% hydrofluoric acid. The PMMA layer seems intact at the base of the vertical nanostructures. c) and d) SEM images of different 3D nanoelectrodes on the same device after dissolving PMMA with acetone. e) wide field SEM image of a pattern of 3D nanoelectrodes after the entire process of SiO_2 deposition, PMMA masking, HF etching and PMMA removal. The sample results not homogeneous.

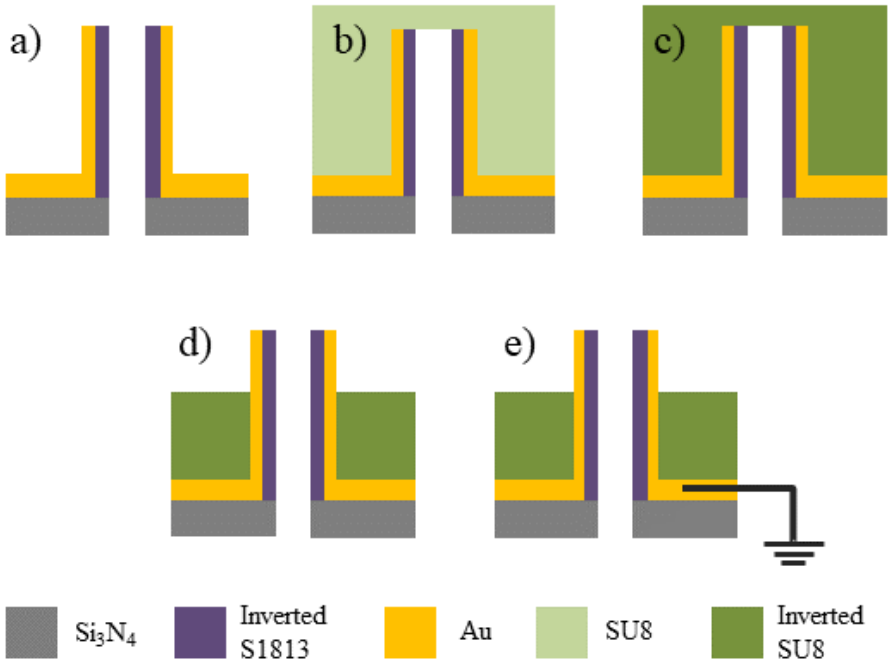

Figure 2.5: Sketch of the passivation process. a) 3D hollow nanoelectrode covered in gold. b) spin-coating of SU8 epoxy polymer on top of the device, c) inversion of the polymer by UV light exposure. d) Plasma etching procedure to make the polymer thinner on the device and e) hard bake of the device and creation of the electrical connection.

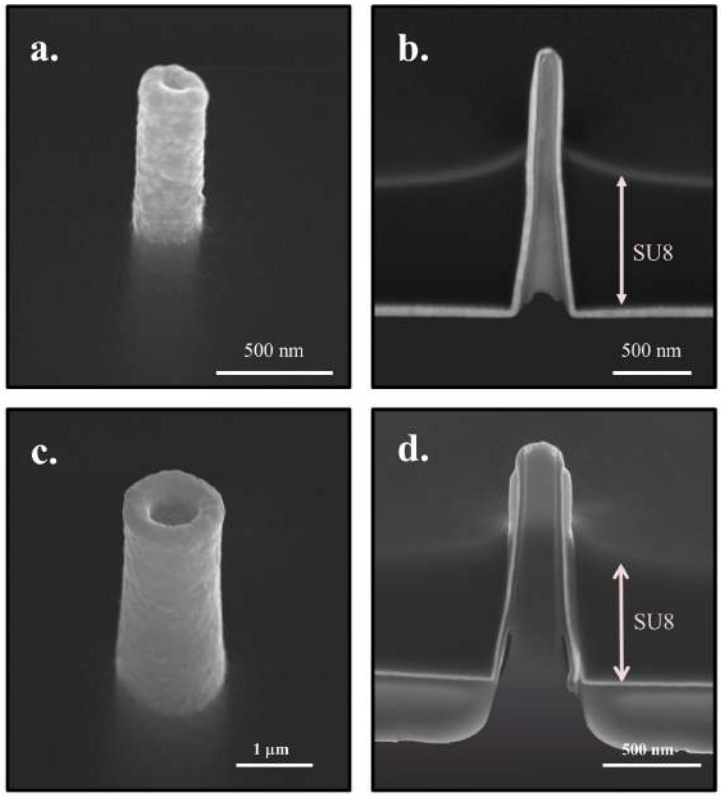

Figure 2.6: SEM images of the finished 3D nanoelectrodes a) and c) are SEM images of the 3D nanoelectrodes respectively of 100 nm (used in the SERS experiments) and 500 nm (used in the delivery experiments) diameter. b) and d) are SEM images of the cross sections of the same 3D nanoelectrodes. The inner nanochannel that connects the two side of the Si_3N_4 membrane is clearly visible.

2.3 Microfluidic chamber and packaging

Since one of the goals of the present research is to deliver molecules inside the porated cells from a separated compartment, a microfluidic chamber has been designed to be interfaced with our device. The microfluidic chamber communicates with the back of the Si_3N_4 membrane allowing molecules to flow through the 3D hollow nanoelectrodes. In this configuration, molecules would be injected from the back side of the membrane - where the molecules are stored - to the front side of the membrane - where the cells are in adhesion with the 3D hollow nanoelectrodes -. An Acrylonitrile Butadiene Styrene (ABS) mold has been designed and 3D printed, so to pour inside it polydimethylsiloxane (PDMS Sylgard 184 elastomer by Dow Corning, Midland, MI, USA). The PDMS has been degassed and cured at 65℃ for one hour to shape the microfluidic chamber, then removed from the mold. The 3D nanostructured Si_3N_4 device is bonded with fresh PDMS to the top of the microfluidic chamber (the back of the membrane facing the inside of the microfluidic chamber) and a glass ring is plasma bonded on top of the microfluidic chamber, so to create a well in which the cells are cultured. A wire is bonded with silver paste to the golden flat surface of the 3D nanostructured device and embedded into the PDMS. The last precaution is essential for two main reasons; first, to avoid toxicity in the cell culture due to silver paste dispersed in the medium, and second to prevent electrical pulses to be delivered from the wire or the silver paste to the cell culture, but only through the 3D nanoelectrode tips. The final microfluidic chamber with the sample mounted on it is shown in figure 2.7.

The 3D nanostructured MEA-like substrates have been exploited without the implementation of the microfluidic chamber. However, a packaging procedure was still necessary in order to create a well in which to grow the cells and to create the electrical connection with an external pulse generator. Each track of the MEA-like device has then been bonded with silver paste to a Printed

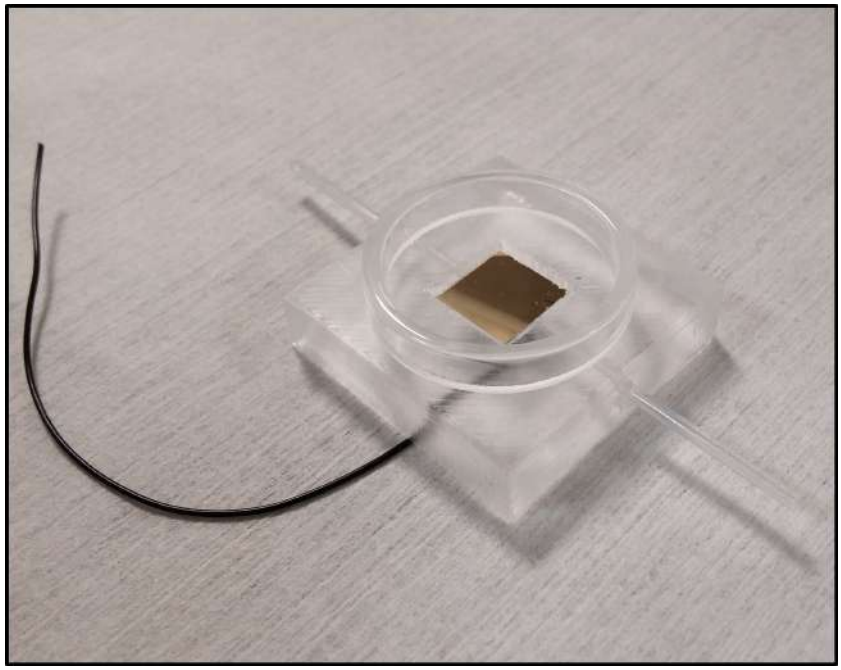

Figure 2.7: Microfluidic chamber with 3D nanostructured Si3N4 membrane mounted at the center.

Circuit Board (PCB) so every flat electrode, patterned with 3D nanoelectrodes, could be individually addressed with an electrical pulse train. A glass ring has been bonded on top of the device with epoxy glue (353NDT) to create the well in which the cells could be grown and to further passivate the device. The resulting platform is shown in figure 2.8.

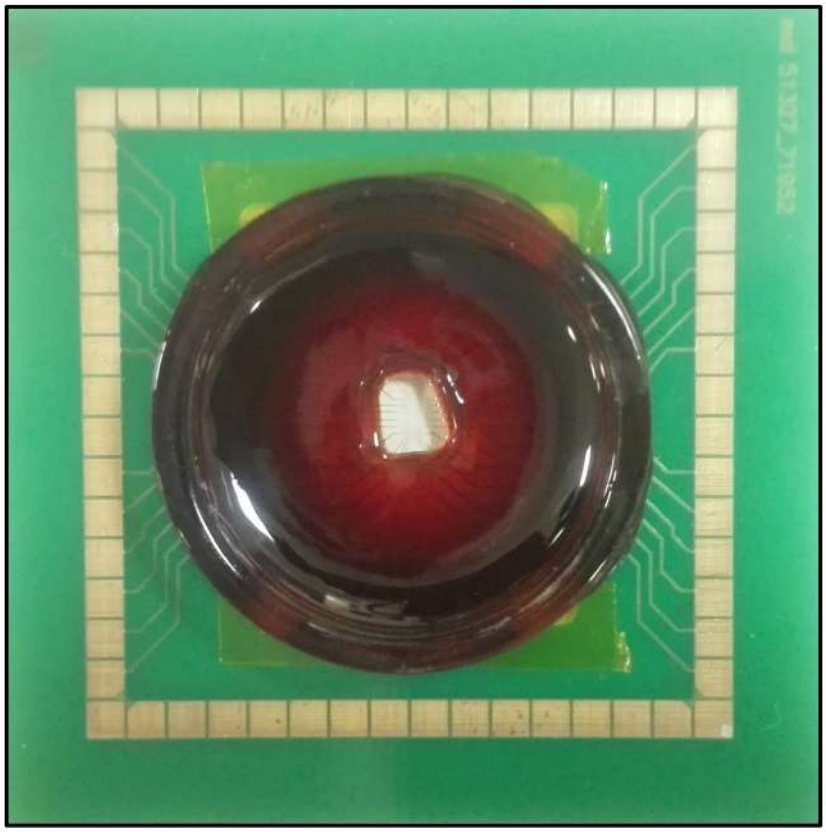

Figure 2.8: Picture of a MEA device bonded to a PCB and packaged in epoxy glue.

2.4 Cell Culture

The cells used to perform most of the *soft-electroporation* experiments and the totality of the SERS experiments are mice fibroblasts NIH-3T3; cardiac cells HL-1 have been used in some of the *soft-electroporation* experiments. Before the seeding of the cells, the devices have been treated with 60 seconds of plasma oxygen (100% O_2, 100 W) to improve their wettability and sterilized with 20 minutes of UV exposure in laminar flow hood. NIH-3T3 cells have been seeded on the devices with a concentration of $1.5 \times 10^4\, cells/cm^2$ in DMEM cellular medium with 1% penicillin/streptomycin (pen/strep) antibiotic and 10% Fetal Bovine Serum (FBS, all by Sigma-Aldrich) and grown at controlled humidity, CO_2 concentration and temperature for 36 hours prior to perform experiments. Before the seeding of the HL-1 cell line, samples have been treated 5 minutes with 0.001% poly-L-lysine solution to increase the cell adhesion on the 3D nanostructured substrate. The samples have been extensively washed with distilled water and dried in sterile condition. HL-1 cells have been seeded at a concentration of $8.5 \times 10^4\, cells/cm^2$ and grown with Claycomb culture medium supplemented with 10% FBS, $100\mu M$ Norepinephrine, $300\mu M$ ascorbic acid, $2mM$ L-glutamine and $100\mu g/ml$ pen/strep antibiotic. Cells have been grown in incubator at 37 ℃and 5%CO_2 concentration with a daily change of culture medium until confluency has been reached. Before the experiments, the samples have been extensively washed in PBS and all the experiments have been performed with cells in PBS. Electroporation of cell membranes has been performed by applying an electrical pulse train between the fabricated 3D nanoelectrodes and a reference platinum electrode immersed in the electrolyte (PBS). The parameters used were a 10 second long pulse train of different amplitudes - depending on the experiments -, with $100\mu s$ long pulses and $20Hz$ repetition rate.

2.5 Fluorescence microscopy

Fluorescence experiments of delivery have been performed using an upright Eclipse FN-1 microscope (Nikon) equipped with a halogen lamp ($50W$). Appropriate excitement light was provided by the addition of specific filters, depending on the desired wavelength. In particular, we injected the impermeable propidium iodide (PrI) dye that is excited at $535nm$ and has the emission wavelength centered at $617nm$, and we used calcein AM permeable dye to assess the viability of the cells after the electroporation; calcein AM has the excitation/emission spectrum centered respectively at $495nm$ and $515nm$. Nikon TRITC filter has been chosen for the detection of the PrI, and Nikon TRIC for the Calcein AM dye. The images have been acquired with a $10\times$ air objective with long working distance ($21.5mm$) and $NA = 0.25$ and with a $60\times$ water immersion objective (Nikon) with $NA = 1$ by means of a camera Hamamatsu Orca Flash R2. Images have been merged and analyzed with ImageJ and GIMP software.

2.6 SERS (Surface Enhanced Raman Spectroscopy)

2.6.1 Experiments

Surface Enhanced Raman Spectroscopy has been performed with a backscattered setup of a Raman spectrometer system (Renishaw inVia). The $\lambda 785nm$ laser has been focused through a $60\times$ Nikon water immersion (WI) objective with numerical aperture of $NA = 1.0$. The 3D nanoelectrodes with the cells wrapped around them have been excited at $0.25mW$ power, to limit the damage to the biological system. Exposure time has been fixed at 1 second and each spectrum is the result of 5 accumulations to improve the signal to noise ratio of the acquisition. In this configuration it has been possible to record automatically one spectrum every 6 seconds on the same 3D nanoelectrode

and on the same cell. The laser power has been kept that low in the attempt of avoiding any stress to the cell under investigation, lasting each experiment 30 minutes of continuous spectral acquisition. Experiments on NIH-3T3 cells have been performed after 2 days in culture (DIVs) removing the cell medium and washing the sample twice with sterile phosphate saline buffer (PBS), the medium in which the experiments have been performed. In situ electroporation has been induced after 10 minutes from the beginning of the experiments through a custom-made micromanipulator that allowed delivering the electrical pulse train without perturbing the setup and the ongoing measurements.

2.6.2 Data analysis

Raman spectra are acquired with WIRE from the Renishaw system, and data analysis of the acquired time-resolved spectra has been performed in Matlab. Color maps are visualized in Matlab or Origin, while single spectra graphs are visualized by Origin. To remove isolated Raman peaks due to cosmic rays interaction with the setup, each single data-set has been interpolated in time using the built-in Matlab function interp2. The time resolved Raman spectra from different experiments have been averaged together to study a collective behavior of the molecular dynamics of the cell membrane in presence of in situ electroporation on the 3D nanostructures. The average intensity of the Raman spectra for each time instant t_i and every wavenumber R_j, has been calculated as

$$\langle I \rangle (t_i, R_j) = \frac{1}{N} = \sum_{s=1}^{N_S} I_S(t_i, R_j)$$

where N_S represents the number of experiments over which the average has been calculated. Two sets of experiments have been performed: they differ from each other only for the presence (or the absence) of the *in situ* electroporation after 10 minutes from the beginning of the experiments. Electroporation

have been performed at $t = 600sec$ delivering a 10 seconds electrical pulse train, being each pulse $3V$ intense and $100\mu s$ long, with a $20Hz$ repetition rate. 10 samples perturbed with the electroporation have been analyzed and averaged together; the results have been compared with the same analysis over 6 experiments in which electroporation has not been applied and the samples remained unperturbed for the whole duration of the measurements (30 minutes). An average in time has been calculated to highlight which peaks have shown changes in time (appearance or disappearance) after the electroporation and different binning times have been evaluated. In the end, an average over the first 10 minutes (*preporation* time) has been compared to bins of 5 minutes after the electroporating event (*postporation* time).

The background of the peaks has been substracted from the measurements after its evaluation. The background estimation algorithm is written in C++ programming language, adopting graphic and analytical libraries of Cern Root Data Analysis Framework. In particular, the TSpectrum Class Reference is used as Advanced Spectra Processing routine. This class contains advanced spectra processing functions for:

- One and two-dimensional background estimation
- One and two-dimensional smoothing
- One and two-dimensional deconvolution
- One and two-dimensional peak search

This function calculates background spectrum from source spectrum. The function allows to separate useless spectrum information (continuous background) from peaks, based on Sensitive Nonlinear Iterative Peak Clipping Algorithm. The sensitive nonlinear peak clipping algorithm is the basis of the methods for estimation of the background in multidimensional spectra, leaving the signal intact.

2.7 Staining and cell cross section

To study the tight sealing of the cells on the 3D nanoelectrodes and on the flat passivated substrate using FIB/SEM cross sectioning, the cells have to be fixed and stained with heavy metals. In this way the lipid and the protein content of the cells will gain enough contrast to be detected by EM analysis.

2.7.1 Staining

Cells have been washed 3 times for 5 minutes in $0.1M$ sodium cacodylate buffer and then fixed with a 2.5% Gluta solution in $0.1M$ Na cacodylate buffer for at least 1hour on ice. Samples have been extensively washed in buffer solution and a RO - T - O staining protocol has been performed. The first step of the protocol involves the staining of the lipid membranes by a reduced osmium solution (RO) for 1 hour on ice. In particular, the RO solution is made of equal volumes of 2% potassium ferrocyanide $[K_4(FeCN)_6]$ and 2% osmium tetroxide (OsO_4); the reduced osmium $(OsFeCN)$ results to be more reactive allowing a better staining of the cellular membranes. The cells are washed three times for 5 minutes in chilled milliQ water at room temperature and filtered 1% thiocarbohydrazide (TCH) in milliQ (T step) has been added for 30 minutes at room temperature. Being TCH osmiophilic, it enhances the staining of the lipids by the osmium. In fact, TCH attaches itself to the previously osmium stained membranes, and allows the deposition of additional OsO_4. The excess of TCH is washed three times with room temperature milliQ and osmium tetroxide (O step) is added for 1 hour at room temperature allowing it to bind to the TCH, enhancing the staining [43].

To stain proteins, nucleic acids and hydroxyl groups in carbohydrates, 5% uranyl acetate filtered solution is added after three washes in milliQ water to the samples and kept overnight in the fridge. Uranyl acetate is washed thoroughly with chilled milliQ on ice, and then increasingly concentrations of

ethanol have been substituted to the aqueous solution (30%, 50%, 70%, 90%, 96% and 100%) on ice, each step lasting at least 15 minutes. The last step has been made at room temperature and repeated once.

Embedding the samples in resin is essential to perform high resolution imaging of the cells and to visualize the cell membranes - nanostructures interfaces. FIB cross sectioning has been preferred to microtome cutting for its higher precision and because it avoids mechanical stress during the slicing process. However, once the sample has been embedded in resin, it is impossible to locate the position of the 3D nanostructure with SEM technique. To overcome this limitation, the samples have been infiltrate in epoxy resin and a recently developed procedure has been added to the protocol to remove the excess of resin from the sample [50], [51], [72].

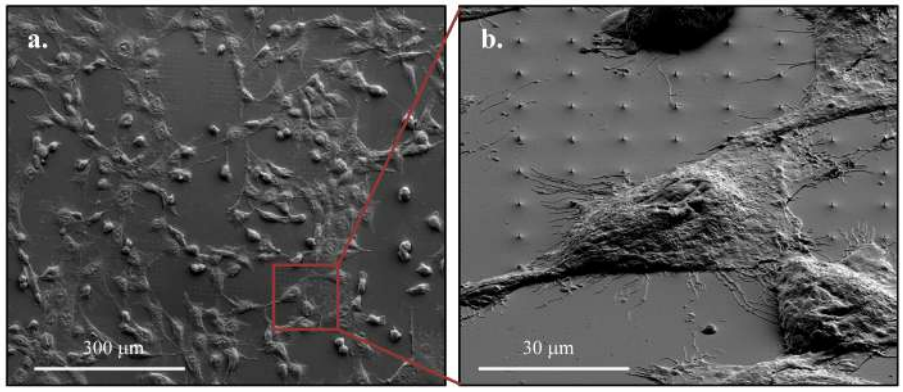

Figure 2.9: SEM images of fixed cells cultured on a 3D nanostructures substrate and embedded in resin. The excess of epoxy resin has been washed away before the polymerization, allowing to see the topography of the cells and to localize the areas of interest on the sample such as the 3D nanostructures. a) overview of the culture and b) zoom in and tilted image (52^o).

Infiltrations of increasing concentration of epoxy resin Spurr in ethanol have been performed (3 : 1, 2 : 1, 1 : 1, 1 : 2, 1 : 3, only resin) for a minimum of three hours each step. The only resin infiltration stage has been performed for at least

24 hours. Each of the stages has been performed in a sealed environment to avoid evaporation of ethanol. The draining of the resin excess has been made by mounting the sample vertically for 1 hour and, prior the polymerization (65℃ overnight), rinsing of the resin excess has been made by pipetting twice with ethanol the samples. The final results are samples in which the cells interior is infiltrated by resin, but the sample topography remains visible by optical microscopy as well as SEM (see figure 2.9).

2.7.2 Cross section and imaging

Each specimen is mounted on a standard FIB stub and it is grounded to it with colloidal silver paste. Samples are sputtered with a thin layer of gold before the imaging to prevent charging during the imaging. A double platinum layer is deposited on the region of interest to preserve the samples and to avoid contamination in the cross sectioned area. The first Pt layer has been deposited by electron-assisted deposition using the gas injection system (GIS) of the dual beam Helios Nanolab 650 (ThermoFischer), while the second layer of Pt has been deposited on top of it with ion - assisted deposition. The electron - assisted deposition is not destructive for the sample, but the average velocity of deposition is low; on the contrary, ion-assisted deposition is considerably faster, especially when high currents are used, but in that case the ionic beam can be destructive, milling the sample faster in respect to the deposition rate.

The first electron - assisted deposition is a sort of sacrificial layer, allowing the use of more energetic ion - assisted deposition without ruining the region of interest. Electron - assisted deposition occurs using a very high current ($6.4\,nA$) and low acceleration beam ($1 - 2\,kV$). In fact, the electron beam - assisted platinum deposition exploits the secondary electrons emitted from the substrate to grow a carbon-rich layer of platinum; the presence of the carbon is due to the incomplete fractionation of the metal-organic precursor gas. The deposition process is driven by the secondary emitted electrons because the

scattering angle with primary electrons is very wide, bringing to a low rate deposition in respect to the secondary electrons that have a narrower scattering angle that allows for efficient Pt deposition; the energy needed for an efficient secondary electron deposition process is around $100\,eV$, depending on the initial acceleration of the electron gun and on the substrate material [73].

Ion-assisted platinum deposition has been performed tilting at 52^o the microscope stage with the sample on it, so to make it perpendicular to the ion gun. The platinum has been deposited with a current of $i = 0.79\,nA$ and beam acceleration of $30\,kV$, while the dwell time has been kept low, in order to use nearly all the injected gas with each beam scan; in this way, the net deposition rate is maximized, minimizing the etching rate of the substrate.

Trenches are milled with a high ion current ($i = 9.3\,nA$) in cross section mode so to expose the part of the cells at the interface with the 3D nanoelectrodes, then a polishing cut with lower current ($i = 0.43$ or $0.79\,nA$) and in cleaning cross section mode has been made.

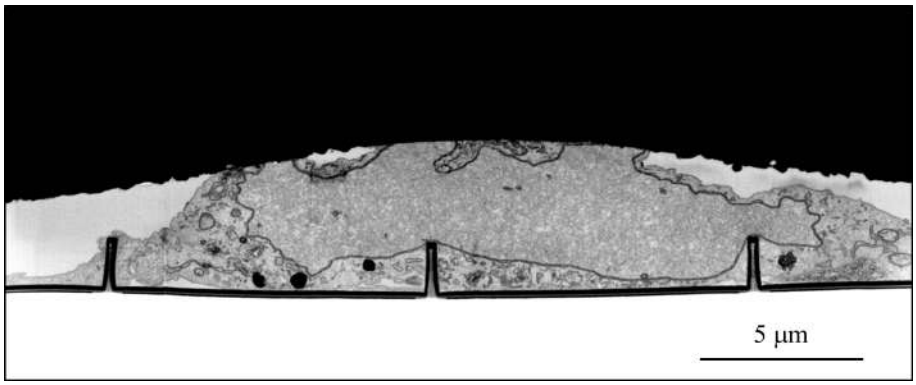

Figure 2.10: SEM image of a FIB cross sectioned 3T3-NIH cell cultured on top of 3D nanoelectrodes without passivation. Colors are inverted in post - production.

Imaging of the cross sectioned cells at the interfaces with the 3D nanoelectrodes have been acquired with the sample still tilted, in immersion mode and

detecting the backscattered electrons with an acceleration of $3\,kV$ and current $i = 0.80\,nA$. Colors have been inverted in some of the cross section images with GIMP to enhance the membrane of the cells and of the organelles (see figure 2.10).

Chapter 3

Soft-electroporation

The surface of the final device is composed by a flat cured SU8 substrate with $700\,nm$ high hollow nanoelectrodes protruding from it; the device is mounted in a PDMS microfluidic chamber and cells are cultured on top of it confined by a glass ring bonded on the PDMS chamber. In this configuration, cells are in contact with the cured flat SU8 substrate and tightly wrapped around the 3D nanoelectrodes, while the molecules to be injected are confined in the underlying PDMS microfluidic chamber separated from the cell culture (see sketch in figure 3.1). The low height of the 3D nanoelectrodes (only $700\,nm$ from the flat passivation) promotes a tight adhesion of the membranes and permits the normal migration and proliferation of the cells during their growth [42], [74], [75].

For the electroporation procedure, cells are washed in PBS (the electrolyte) and a platinum counter-electrode is immersed in the electrolyte. The counter-electrode is connected to a pulse generator together with the wire contacting the 3D nanoelectrodes and embedded in the PDMS microfluidic chamber. The sample is placed under an upright microscope and imaged in both bright field and fluorescence in this configuration. The microfluidic chamber below the sample is filled with a solution containing 0.1% of propidium iodide in PBS.

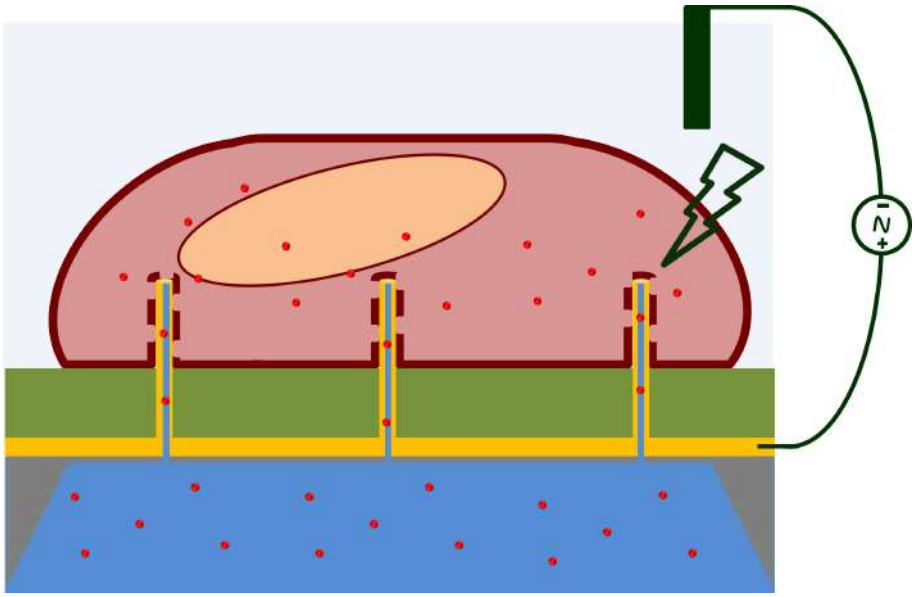

Figure 3.1: Sketch of the soft-electroporation system. Cells are in tight adhesion with the entire substrate: in yellow the 3D nanoelectrodes covered in gold while in green there is the SU8 passivation layer. When a pulse train is applied to the cell culture, nanopores are opened at the interface with the 3D hollow nanoelectrodes. The molecules that are initially stored in the separated compartment beneath the cell culture are now free to diffuse through the 3D hollow nanoelectrodes inside the cells.

A pulse train with $20Hz$ repetition rate is applied for 10 seconds to the sample; each pulse is $100\,\mu s$ long with an amplitude of $2\,V$ (*soft-electroporation* protocol).

Since the cells are in tight adhesion with the 3D nanoelectrodes and being the platinum counter-electrode few mm away from the electrically active area of the device, an applied pulse train of $2\,V$ in amplitude and few μs long is sufficient to generate a *trans-membrane* voltage high enough ($> 1\,V$) to open nanopores in correspondence of the 3D nanoelectrodes tips, but not far away from it. The molecular structure of the plasma membrane is then locally rearranged, hydrophilic nanopores are generated and rapidly filled with aqueous medium. Since the permeabilization is generated on the membrane in contact with the 3D nanoelectrodes, the only liquid available to fill the nanopores is the one that comes from the underlying microfluidic chamber that contains the molecules to be delivered. In fact, the portion of the cell membrane that is not in close contact with the 3D nanoelectrodes, that is all the cell exposed to the electrolyte or adherent to the SU8 substrate, will feel a weaker *trans-membrane* potential and will not undergo to permeabilization. Propidium iodide is delivered in the electroporated cells, staining them in red when it intercalates in the DNA double strand. It also has a low affinity for RNA and single strand DNA, showing a background in the cytoplasm. 3T3-NIH cells electroporated and delivered through different spatial arrangement of the 3D hollow nanoelectrodes are showed in figure 3.2.

In this configuration, the setup allows to have selectivity over the cells that become temporary accessible, being only the electroporated ones those to be delivered with exogenous molecules. In addition, having a microfluidic system connected to the sample allows the perfusion of heated medium below the cell culture, maintaining a basal temperature during the experiments. Calculations about the amount of delivered molecules through the nanoelectrodes have been performed using the software COMSOL Multiphysics in previous work [10],

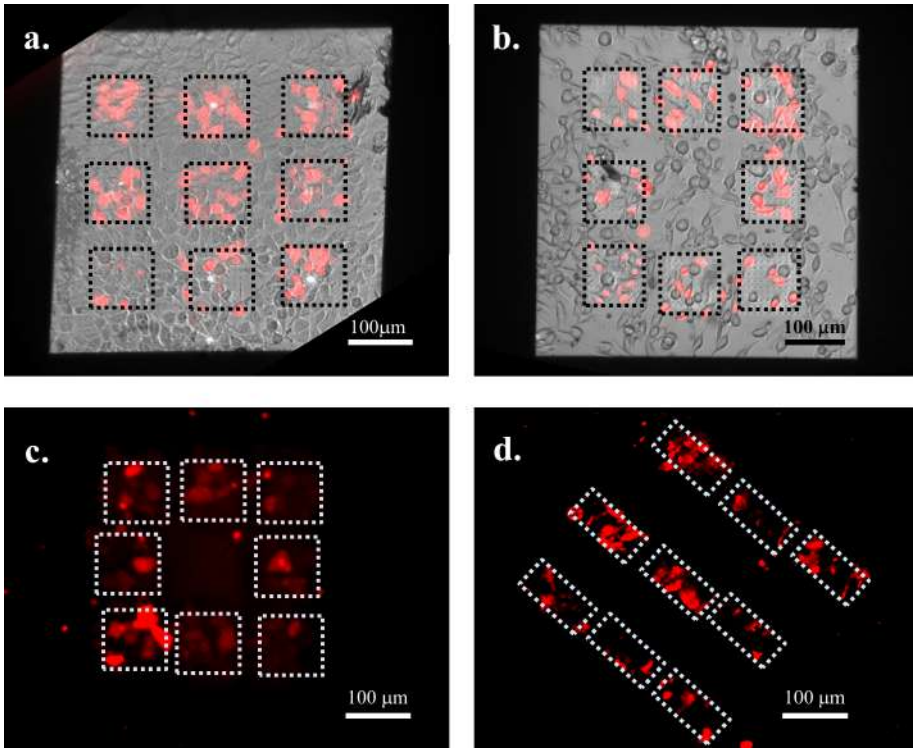

Figure 3.2: 3T3-NIH cells on top of different arrangement of 3D nanoelectrodes arrays on Si_3N_4 membranes. The cells have been electroporated and propidium iodide (in red) diffused inside the porated cells from the separated microfluidic chamber. Only the cells that grew on top of the 3D nanoelectrode arrays have been electroporated and stained.

leading to the result of 10^6 molecules/minute. These calculations consider an initial concentration of the propidium iodide dye of $1.5 \times 10^{-3} M$ and are developed using a pure diffusion model as

$$\frac{\partial c}{\partial t} + \nabla \cdot (-D \nabla c) = R.$$

In the diffusion equation, c is the dye initial concentration, R is a source term and D is the diffusion coefficient of the dye in aqueous solution (such the PBS); it was derived by the relation $D = (k_B T)/6\pi\eta r$. Here, k_B is the Boltzmann constant, temperature T was set to $300\,K$, the dynamic viscosity of the PBS solution was considered $\eta = 1 \times 10^{-3} Pa \cdot s$, and r is the dye average radius. The so calculated diffusion coefficient is $D = 2.1 \cdot 10^{-10} m^2/s$, in accordance with experimental results previously found in literature [5]. Viability tests have been performed to confirm the well - being of the cell culture, and permeable Calcein AM (that becomes green when processed by live and healthy cells) has been administered for this purpose. Figure 3.3 shows details of fluorescence images of PrI delivery and viability tests.

To prove that the nanopores on the plasma membrane are opened only in correspondence of the 3D nanoelectrodes, experiments in which Propidium iodide was added directly in the cell culture were performed. Since the dye is impermeable to the cell membrane, only dead or apoptotic cells presented the red staining after the addition of the Propidium iodide in the culture well and before the electroporation. Then, when the electroporation protocol was applied, the lack of additional stained cells proved that no cells were presenting nonspecific permeabilization over the plasma membrane, but only permeabilization in proximity of the 3D nanoelectrodes (see figure 3.4). These experiments also proved that the cells are tightly sealed to the substrate and to the 3D nanoelectrodes, preventing molecules from the cell bath to infiltrate between the lipid bilayer and the substrate.

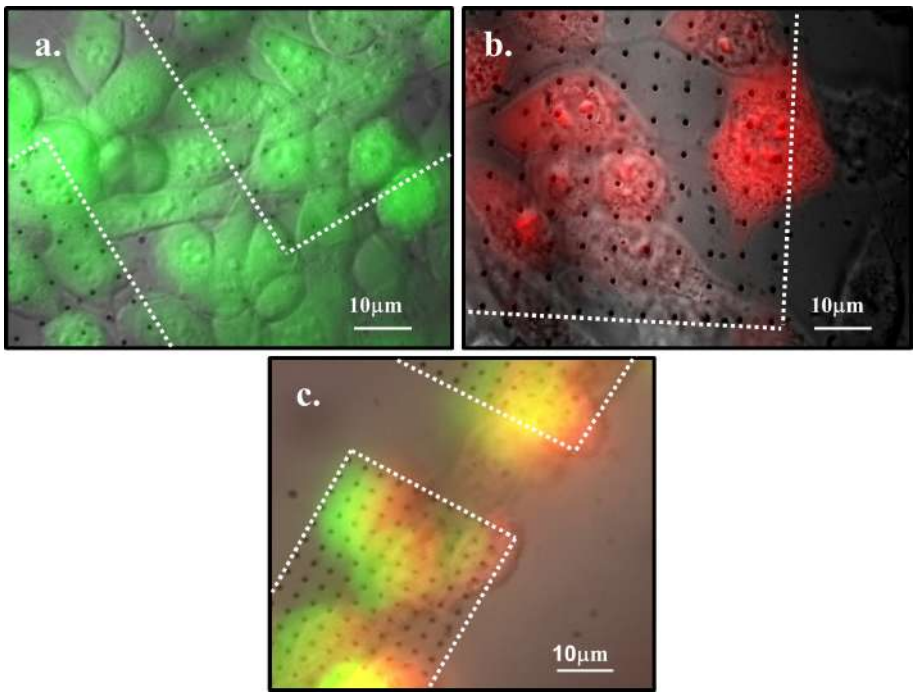

Figure 3.3: Detail of cells on 3D nanoelectrodes. a) Viability test performed with permeable dye Calcein AM. b) *Soft-electroporated* cells have been stained by Propidium iodide injected through the 3D hollow nanoelectrodes. c) viability test with permeable dye Calcein AM in the culture well after *soft-electroporation* and delivery through 3D hollow nanoelectrodes have been performed.

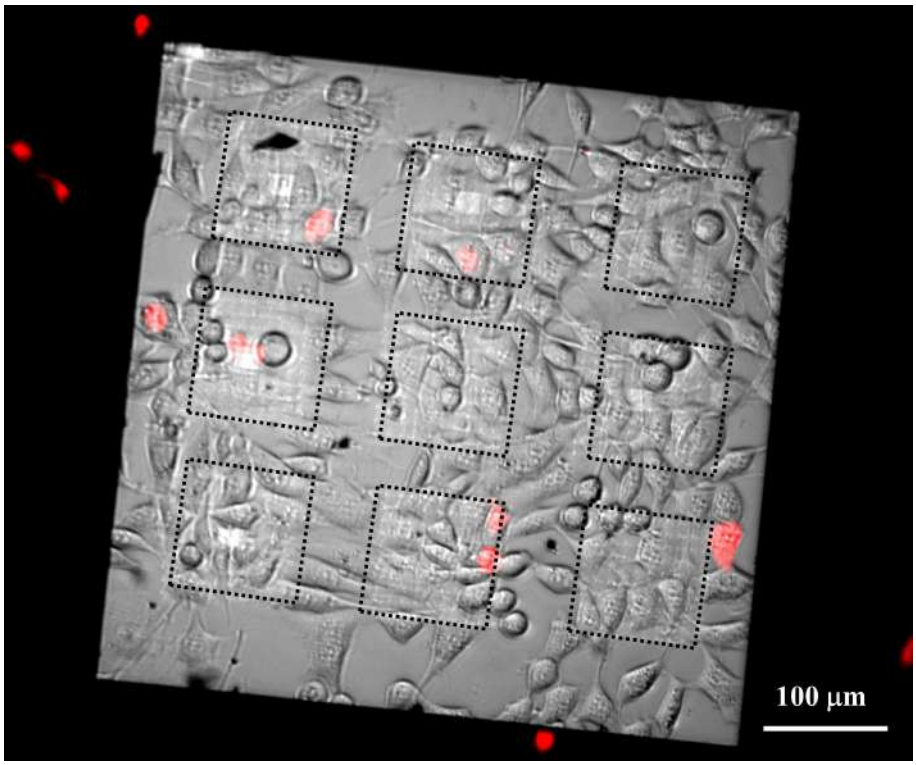

Figure 3.4: Propidium iodide has been added to the cell culture well and then *soft-electroporation* has been performed. The number of stained cells did not increase because nanopores on the plasma membrane have been opened only in contact with the 3D hollow nanoelectrodes and the cells present a tight sealing with the substrate, avoiding molecules to penetrate from the cell bath.

The soft-electroporation protocol consists in 200 electric pulses delivered with a frequency of $20Hz$ for 10 seconds, each pulse lasting $100\,\mu s$ and $2\,V$ in amplitude.

When the soft-electroporation protocol was performed, the statistic showed a $> 80\%$ efficiency of molecules delivered in the cells that lied on top of the 3D nanoelectrodes, with a standard deviation of 7% and cell viability $> 98\%$. These results are calculated on 6 experiments with NIH-3T3 cultured on different devices; for each experiments the number of cells that are lying on the 3D hollow nanoelectrodes arrays has been considered.

The NIH-3T3 cell line is a good system to test and to develop a technique because these kinds of cells are easier to treat and to grow in respect to other cell lines and especially in respect to primary cells. Cardiac muscle cells are used as test systems in several studies both in medicine and in electrophysiology because of their electrical activity that mimics neuronal action potentials. Cardiomyocytes require more attention and are harder to deliver respect to fibroblasts such as NIH-3T3; in this regard, once the micro - nanofluidic electroporating system was developed and the soft-electroporation protocol established, it was tested on HL-1 cardiomyocytes. The developed platform and poration protocol was able to successfully target HL-1 cells and to deliver molecules inside the electroporated cardiomyocytes with an efficiency slightly inferior to the previous study (see figure 3.5 a). However, raising the amplitude of the delivered pulses ($3\,V$), the efficiency is restored to the values reached with the *soft-electroporation* protocol applied to NIH-3T3 cell line.

The 3D nanostructures are combinable with flat electrodes in MEA-like devices [24], [68], [76] that can record electrical signals and interact with individual cells due to their comparable dimensions ($5\mu m$ in diameter). Addressing a single cell at the time can be interesting for multiple applications not only in electrophysiology but also in the study of cell behavior after the uptake of molecules from the environment. Delivering different molecules in adjacent

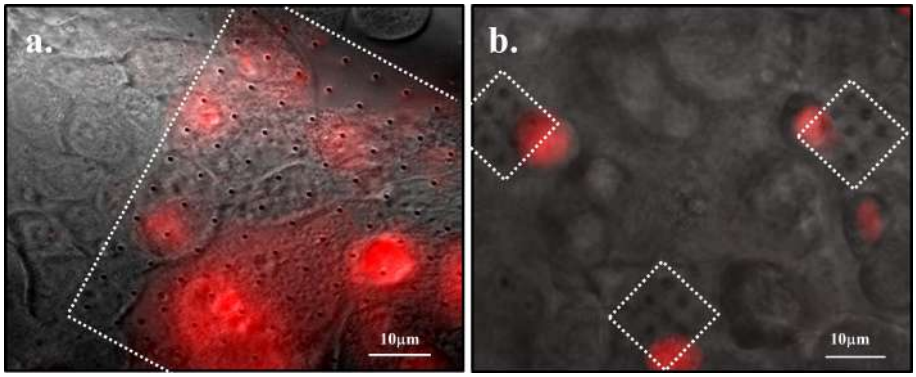

Figure 3.5: a) Cardiomyocytes HL-1 *soft-electroporated* and delivered with Propidium iodide through the 3D hollow nanoelectrodes in conditions similar to 3T3-NIH cells, and b) on smaller 3D nanoelectrodes arrays that mimics the dimension of a single cell.

cells can be interesting for unravelling intercellular interactions or to stimulate different responses within the same cell culture.

To investigate the possibility of single-cell delivery, smaller arrays of 3D nanoelectrodes were fabricated with dimensions that matched a single cell ($10\mu m \times 10\mu m$), being each array far away from the others ($50\mu m$). When the electroporation was performed and molecules were delivered in this configuration (see figure 3.5 b), single cells were successfully addressed.

The *soft-electroporation* protocol is similar to a previous work that exploited the nanopores on the plasma membrane to get access to the intracellular electrical activity of cardiomyocytes and to record it [14]. This particular study is one of the few that uses voltages as low as the one needed for the electrolysis of water molecules and is designed to record action potential from the adherent cells; however, it is not able to deliver molecules to the targeted cells. The 3D nanopillars are in fact bulky and without an inner nanochannel that could communicate with a separated compartment.

When comparing the present work with other similar studies in which de-

livery has been performed [25], it can be noticed that the *soft-electroporation* achieves the same results and success rate using a much lower applied potential due to the adhesion of the cell membrane with one of the electrodes of the system. This configuration reduces drastically the formation of ROS in the cell bath, increasing the long-term healthiness of the cell culture.

Experiments with higher applied voltages have been performed. Above $4 - 4.5\,V$ the formation of electrolytic gas bubbles has been detected on the tip of the 3D nanoelectrodes. After the pulse train ended, the bubbles disappear in few seconds but the cells resulted to be damaged.

Chapter 4

Cell-3D nanoelectrode interface

To better understand the interaction between the cells and the 3D nanostructures and to confirm the tight sealing that the cells exhibit with the presented substrate, the adhesion of cells on the 3D nanoelectrodes arrays has been studied with ionic beam ablation together with electron microscopy imaging.

NIH-3T3 cells have been grown on passivated 3D nanostructured substrates and processed to be imaged by electron microscopy. The recently developed preparation technique [50], [51], [72], [77], exploits the hard staining of the cell membranes by heavy metals (osmium and uranyl acetate) and the embedding in resin of the whole sample as in the transmission electron microscopy (TEM) preparations. The final step however differs from the classical preparation technique, allowing the sample to be imaged by scanning electron microscopy (SEM) because most of the resin has been removed and it remains only in the intracellular compartments.

Whit this new preparation it is possible to visualize the region of interest (ROI) where the 3D nanostructures are located and to identify the best cells

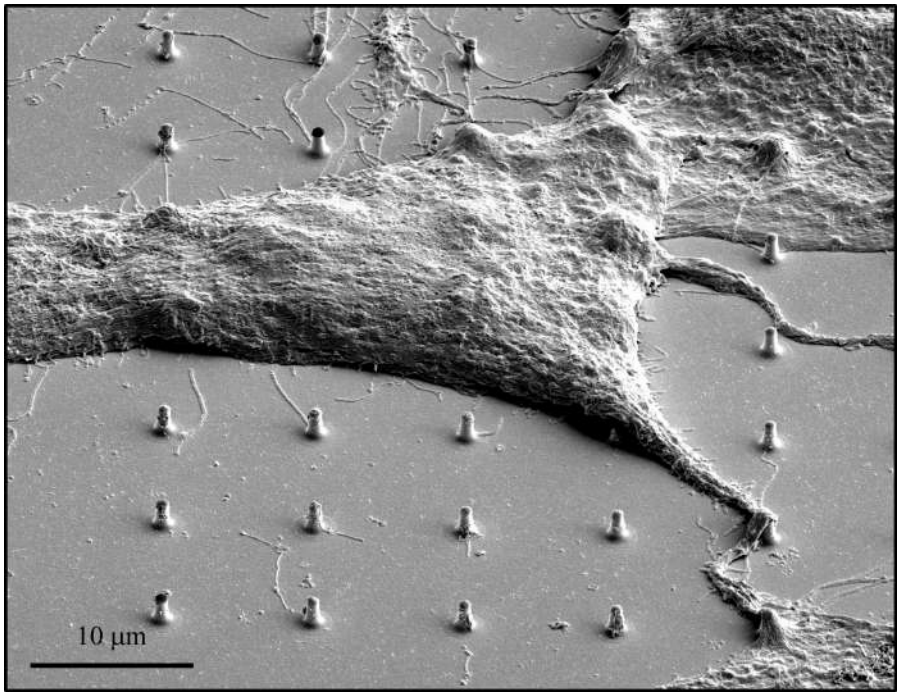

Figure 4.1: SEM image of a NIH-3T3 cell grown on top of an array of large 3D nanoelectrodes (400 nm in diameter), prepared following the described protocol.

to analyze.

Normally, in dealing with resin embedded cellular samples, the specimen needs to be cut in advance with a mechanical method (microtome) and then all the slices have to be imaged until a suitable region has been found. Alternatively, performing FIB cross sections using a dual beam equipped with a SEM there is no possibility of locating the ROI in a resin embedded cell sample before performing the slicing. For this reason, the recently developed method in which the resin excess is removed from the sample before the polymerization [51], [72] is revolutionary and extremely useful when the topic of interest is the interface between nanometer structures and biological samples (see figure 4.1 in which the ROI is clearly visible with the 3D nanoelectrodes protruding from the flat substrate and the cells that lies on top of them).

The improvement in respect to TEM imaging is that the samples no longer require to be sliced with mechanical methods that could break the substrate in a not controlled way; moreover, is possible to perform very thin slices of the sample without damaging neither the 3D nanostructures nor the cell membranes in adhesion on them.

NIH-3T3 cells have been fixed after 36 hours in culture and the staining protocol previously described has been performed on the samples. In the end, the specimens were mounted on standard FIB stubs and glued to them with silver paste to allow the grounding of the specimens. A thin layer of gold has been sputtered on them and the cutting and imaging process has been carried out.

In figure 4.2 the same cell is imaged from the top and with the sample tilted at 52^o before the FIB cutting in correspondence of the dotted line. Panel c is the SEM image acquired with a backscattered detector of the cell cross section; all the substrate layers are clearly visible, from the gold at the base and on the 3D nanoelectrodes (in black because of the inverted colors) to the SU8 passivation layer (in white) that covers half of the vertical gold nanoelectrodes. The cell

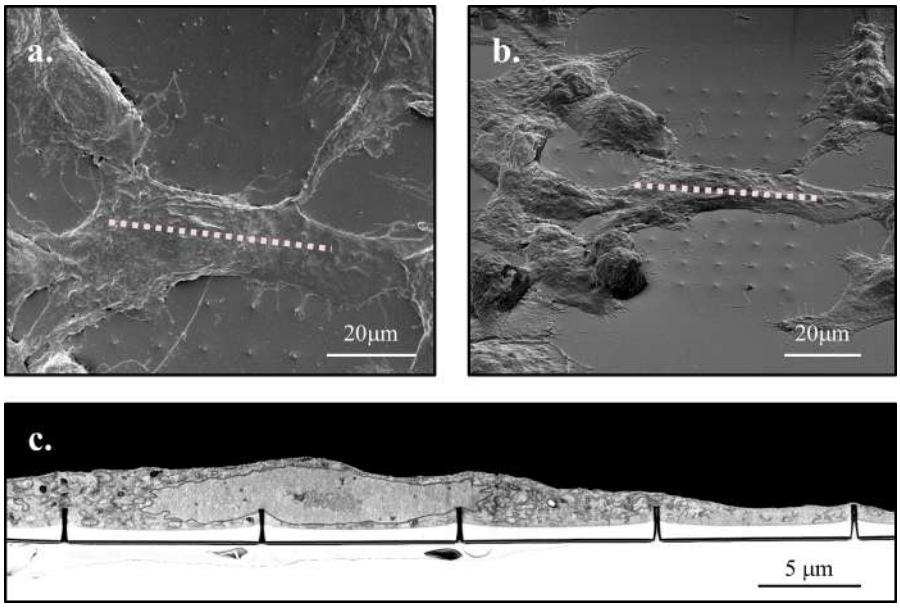

Figure 4.2: a) SEM image of NIH-3T3 cells grown on small (150 nm in diameter) 3D hollow nanoelectrodes array, fixed, stained and embedded in resin with the protocol previously described. b) SEM image of the same ROI tilted at 52^o before the deposition of the platinum and the trench of the sample. The dotted lines represent where the trenches have been milled. c) SEM image of the FIB cross sectioned cells in correspondence of the dotted lines in a) and b). The colors in the cross section SEM image are inverted to improve the visualization.

nucleus is visible with denser regions of chromatin in the central part. The double envelope that contains DNA seems to lean on the 3D nanoelectrodes and the nucleus is accordingly deformed. Looking in more detail around the vertical protruding nanostructures, the plasma membrane can be seen in close contact with the 3D nanoelectrode, as shown in figure 4.3, demonstrating that there is no impaling process or spontaneous penetration of the cell membrane as previous studies suggest [78].

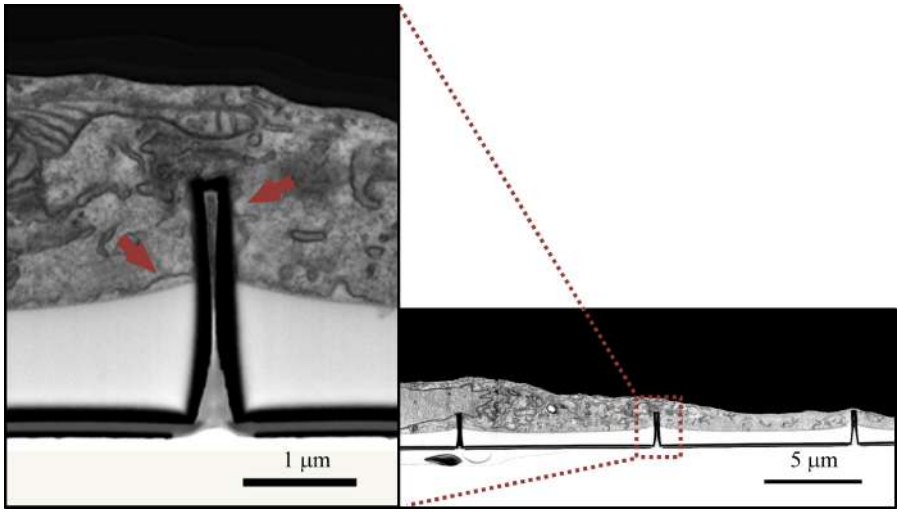

Figure 4.3: SEM backscattering image of the cell membrane tightly wrapped around one 3D nanoelectrode on a SU8 passivated substrate. The arrows indicate the plasma membrane tightly wrapped around the vertical nanoelectrode. On the right, a bending of the membrane can be ascribable to a clathrin-mediated endocytosis event. Colors in the SEM images are inverted.

The cell membrane is tightly sealed both on the flat SU8 substrate and around the 3D nanoelectrode, guaranteeing a very high and localized *trans-membrane* potential when an electrical pulse train is delivered and promoting the local permeabilization of the cell.

From the inset in figure 4.3 and 4.4 it is also visible the inner nanochannel of

the 3D nanoelectrode, through which molecules are delivered from the bottom part of the device (the microfluidic chamber).

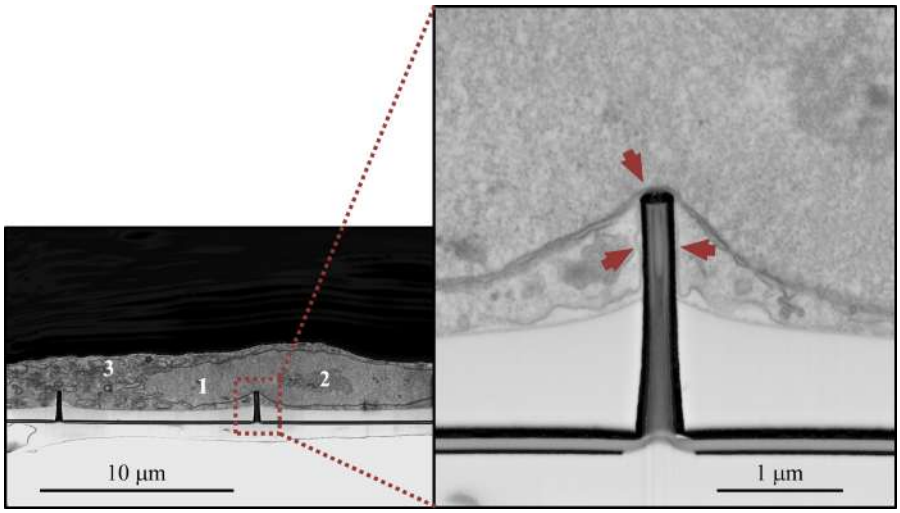

Figure 4.4: SEM cross section image of a cell on top of a 3D nanoelectrodes substrate passivated with SU8. Nucleus (1), nucleolus (2) and mitochondria (3) are identifiable from the image. The inset is the single 3D hollow nanoelectrode embedded in the SU8 passivation. In this particular cross section, the nuclear double envelope is well defined (top arrow) and it can be seen how it follows the contour of the tip of the nanoelectrode coming in close contact with it. The plasma membrane instead, tightly wraps the whole vertical nanoelectrode all the way down to the flat substrate (bottom arrows), to which remains in close contact. Colors in the SEM images are inverted.

When slicing through a 3D nanoelectrode in correspondence of the nucleus of one cell, it is possible to investigate the different behavior between the plasma membrane, that divides the cellular cytoplasm from the surrounding, and the nuclear envelope that is composed by two lipid membranes separated from each other of approximately $20 - 40\,nm$, creates the perinuclear space and separates the genetic material from the cytosol [79]. The nuclear envelop eases down on the 3D nanoelectrode tip, but presents just a soft bending around the edges and then "floats" in the cytoplasm trying to maintain its original shape [72]

(see figure 4.4). On the contrary, the plasma membrane is in close contact with the 3D nanoelectrode following closely its contours all the way down to the SU8 planar passivation. Small curvatures ascribable to clathrin-mediated endocytosis events [42], [72] are visible around the vertical nanostructures and at the interface with SU8 (see insets of figures 4.3 and 4.4).

The proximity of the nuclear envelope to the 3D nanoelectrodes suggests the possibility of electrically porate also the double membrane that contains the genetic material, and to have access to a completely new set of information.

Chapter 5

Membrane dynamics during electroporation

Once the platform able to electrically porate the cellular membrane in correspondence of the nanoelectrodes tips has been developed, it has been possible to blend this technology with the plasmonic proprieties of the 3D vertical nanoelectrodes. In this regard, by shaping properly its geometry, the nanostructure can be coupled with a near infrared laser (NIR) and act as an enhancer for Raman signals through the plasmonic proprieties of the gold. The spectroscopic capabilities of the 3D nanostructures have been largely studied in the past years [80] together with their coupling and efficiency in detecting cellular samples spectroscopic fingerprints [62]. The idea is to exploit the plasmonic characteristics of the device to investigate the dynamics of a cell in adhesion on it before, during and after *in situ* electroporation.

Since for these kinds of study there is no need to deliver molecules inside the cells, the device has been fabricated slightly differently from the one used in the delivery experiments; namely, the 3D nanoelectrodes have been fabricated on a bulk piece of quartz so that they do not act as a nanochannels. The sample

is a MEA-like device with 24 gold electrodes on which 3D nanoelectrodes have been fabricated; the whole sample is also passivated with SU8 so that only the 3D nanotips of each electrode result electrically active. Thus, the cell - nanostructure interface closely resembles that of the delivery experiments, allowing for the use of the same *soft-electroporation* protocols. NIH-3T3 cells have been seeded and grown in the packaged samples and experiments are performed with cells at confluency in the culture well. Cells have been washed in PBS and the sample has been placed under the microscope equipped with the Raman spectrometer; the micromanipulator has been arranged accordingly on the optical table to connect the chosen electrode on which electroporation has to be performed.

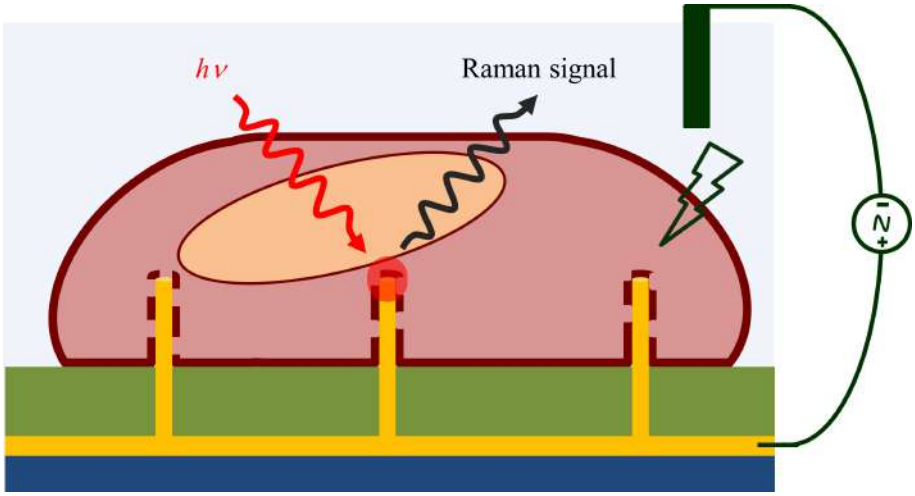

Figure 5.1: Sketch of the system. Cells are wrapped around the 3D nanoelectrodes and the electric pulse is applied to open nanopores on the cellular membrane. A laser is focused on the tip of one 3D nanoelectrode that enhances the Raman modes of the molecules close to the hot spot, and the Raman signal is recorded.

The Raman signal is excited by focusing the $\lambda = 785\,nm$ laser on the tip of a 3D nanoelectrode with a cell on it; the enhanced Raman spectra are recorded

for 30 minutes. A sketch of the setup is shown in figure 5.1. Each recording is the accumulation of 5 spectra acquired with 1 second of laser excitation to maximize the signal to noise ratio, maintaining a high temporal resolution in respect to the investigated time-window.

Electroporation of the targeted cell has been performed during the experiments by applying a potential difference between the 3D nanoelectrodes and a platinum reference electrode immersed in the cell bath. Electroporation was always performed 10 minutes after the beginning of the Raman acquisition. This procedure allows having 10 minutes of cell membrane dynamics "at rest", meaning with no external stimuli, and 20 minutes of cell membrane dynamics recordings after the aperture of nanopores. Because the Raman signal is enhanced enough to be detected only in a very small region around the plasmonic hot-spot, that is the nanoelectrode tip, the recorded spectra follow the rearrangement dynamics of the plasma membrane in close contact with the it. The parameters used to open the nanopores are similar to those of the *soft-electroporation* protocol [15]. In particular, the amplitude of the pulses has been set to $3\,V$ being each pulse $100\mu s$ long with $20Hz$ of repetition rate; the pulse train has been kept on for 10 seconds delivering a total of 200 pulses.

In figure 5.2 three enhanced Raman spectra recorded at the interface with a 3D plasmonic nanoelectrode and a cell wrapped to it are shown. The spectra have been acquired from the same nanoelectrode tip in different time moments of the recording. In particular, the black spectrum is the acquisition after 5 minutes from the beginning of the measurements but before any external stimuli have been applied to the sample; its Raman peaks are then related to molecules presents in the plasma membrane in close contact with the 3D plasmonic nanoelectrode when the cell is in its basal conditions. The red spectrum however, is recorded in the same spatial position but after the application of the electroporating pulse train that opened nanopores in the plasma membrane.

Some of the peaks that appear in the Raman signal are much more intense

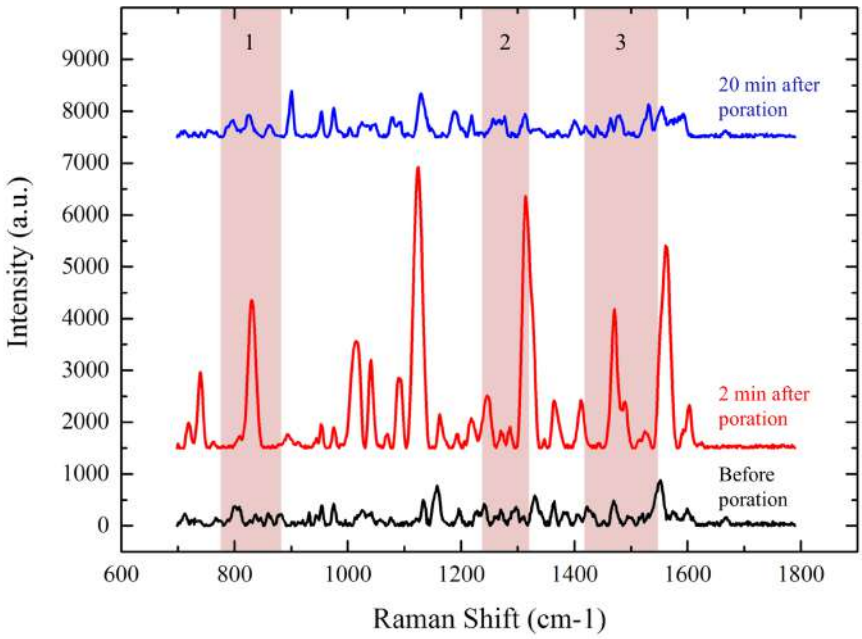

Figure 5.2: Raman spectra recorded from the same 3D plasmonic nanoelectrode before (black), 2 minutes after the application of the electroporation pulse train (red) and 20 minutes after the application of the electroporation pulse train (blue). Three regions of the Raman shift are highlighted in which there are a majority of peaks related to lipids (1 and 3) and proteins (2). The background of the spectra has been subtracted and the intensities coherently shifted to improve the visualization. Data from a single experiment.

in respect to those recorded before the electroporation. That could be related to the increase in number of the molecules close to the 3D plasmonic nanoelectrode, or to the molecules having moved closer to the hot-spot of the nanostructure during the rearrangement that follows the permeabilization. Interestingly, the majority of new and intense peaks are confined in the shift regions (numbered with 1, 2 and 3) that contain the vibrational modes of mostly lipid [81] ($780 - 890\,cm^{-1}$ and $1400 - 1550\,cm^{-1}$) and protein [82] ($1240 - 1310\,cm^{-1}$) related molecules. After 20 minutes from the electroporation pulse train application, the blue spectrum in figure 5.2 shows a decrease in the intensity of the peaks, and the disappearing of the majority of the proteins related modes that were visible after the permeabilization of the membrane, suggesting that the lipid bilayer is completely reformed having close all the nanopores.

Some of the experiments have shown a loss in the signal after the application of the electroporation, while others spectra exhibited an increase in the signal intensity; the reason being the different position of the cell on the 3D nanoelectrodes. The following graphs are color maps of time-resolved measurement over 35 minutes of acquisition. On the x-axis the wavenumber k, or Raman shift in cm^{-1} is represented, while on the y-axis there is the time. The different colors are different intensities of the signal, from the low intense in blue, to the most intense in red/dark red.

It has been noticed that when the plasma membrane is wrapped around the 3D nanoelectrode and is also tightly attached to the flat substrate around it, on average the signal following the electroporation increases in intensity (see figure 5.3 a, b). On the contrary, when the tight sealing between the 3D nanoelectrode and the cell is limited only to a part of the membrane (see figure 5.3 d), the initial spectrum results lower in intensity and an electroporating event will cause the loss of the signal with no recovery in time.

The best hypothesis to explain these behaviors is that, if the membrane is floating on the 3D nanoelectrodes, *in situ* electroporation will cause the

membrane to detach from the 3D plasmonic hot-spot (see figure 5.3 c, d). On the contrary, when the cell is tightly adherent around the 3D nanoelectrode, an electrical pulse train will increase the adhesion tightness.

To find an average behavior of the cell membrane dynamics during the *in situ* electroporation, the spectra of 10 samples in which the nanoelectrode was in contact with a central part of the cell, and not at the edge, have been averaged together and plotted in figure 5.4 c. The acquisitions have been made along 30 minutes, one acquisition each 6 seconds with electroporation performed after 10 minutes from the beginning of the experiments ($t = 600\,s$, represented by the dotted line in the color map) and lasting 10 seconds (2 acquisitions). The resulting graph has been compared with the average spectra of samples in the absence of the electroporation during the recordings (figure 5.4 a). The presence of an electroporation pulse train changed dramatically the Raman response of the samples, while the Raman peaks remained stable in time when no external stimuli have been applied, suggesting that the measurement did not affect the system dynamics during the whole experiment.

The excitation laser power is very low (around $0.25\,mW$) and the excitation wavelength is in the near infrared ($\lambda = 785\,nm$) to minimize the interaction with the biological samples and the cell degeneration [57]. The not porated samples present stable peaks in time and in intensity, with only few single spectra with more intense peaks over the whole Raman shift. This kind of behavior can be related to the dynamics of the cell membrane that move closer to the 3D plasmonic nanoelectrode, allowing a higher enhancement of the vibrational modes of the plasma membrane molecules. Nevertheless, such behavior is not comparable with previous studies because of the lack of similar time-resolved measurement on living in vitro systems. Most of SERS studies on in vitro cells are in fact performed on fixed specimens [83], [84], while those that measure the SERS of living cells, usually acquire a single spectrum and do not study the plasma membrane dynamics during long period of times [66], [85]. When

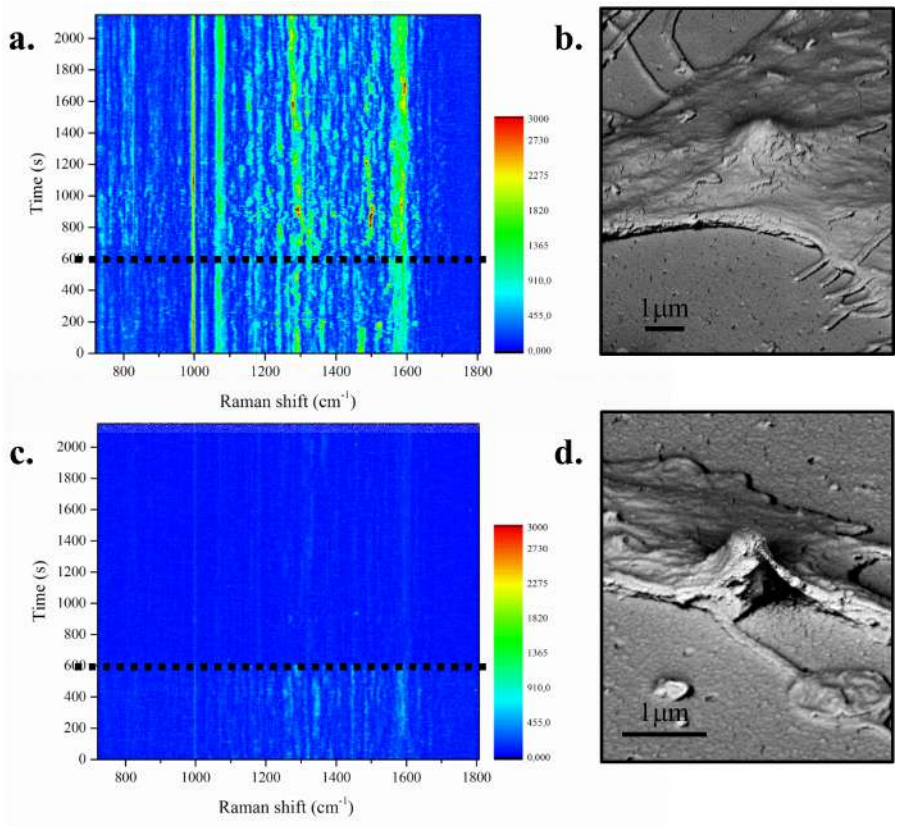

Figure 5.3: a) time-resolved Raman enhanced acquisition over 35 minutes of time coming from a 3D nanoelectrode in contact with a central part of the cell membrane. After 10 minutes electroporation protocol is applied (dotted line); the signal increases in intensity, new peaks appear and other start to shift in wavenumber. b) SEM image of 3D nanoelectrode with a cell on top of it tightly wrapped. The cell membrane is also in adhesion with the flat substrate surrounding the 3D nanoelectrode. c) Time-resolved Raman enhanced acquisition over 35 minutes of time coming from a 3D nanoelectrode in contact with a cell edge. The initial spectrum is lower in intensity respect to the previous; after 10 minutes electroporation protocol is applied (dotted line) and the signal disappears and do not recover in time as if the cell moved away from the 3D nanoelectrode. d) SEM image of a 3D nanoelectrode in contact with a cell edge. The cell membrane is not tightly sealed all around the 3D nanostructure.

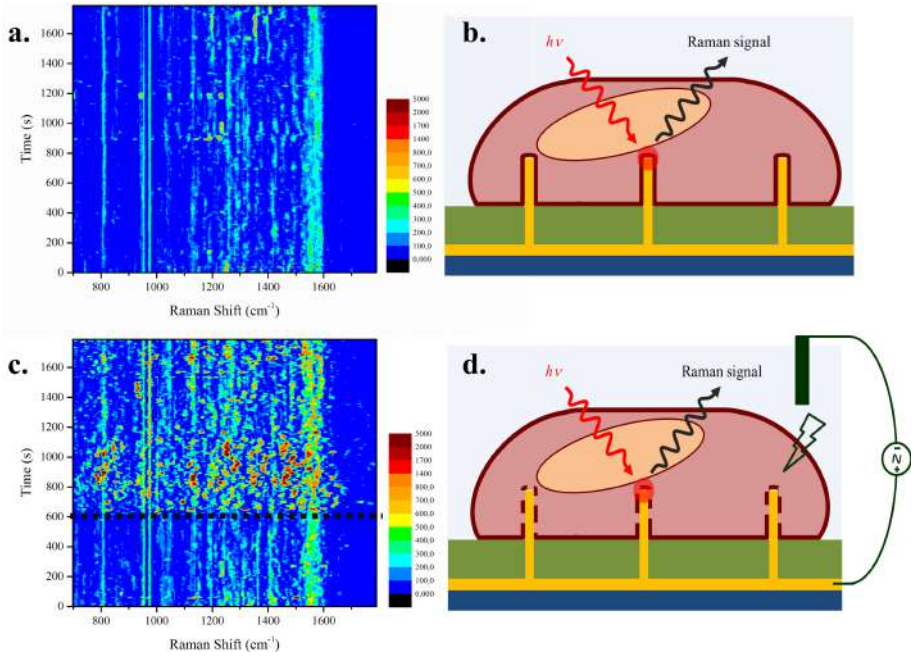

Figure 5.4: a), c) Color maps of the time-resolved average Raman enhanced spectra of cell membrane dynamics in contact with a 3D plasmonic nanoelectrode with b), d) the relative sketches of the conditions. The $\lambda = 785\,nm$ laser excites a 3D plasmonic nanoelectrode and the acquisition have been taken every 6 seconds (5 accumulations of 1 sec acquisition) during 30 minutes of recording. a) average of 6 experiments without the application of external stimuli. c) average of 10 experiments with an electroporation pulse train applied at $t = 600\,sec$ and 10 seconds long after the beginning of the measurements (dotted line). The background has been subtracted to the original acquisitions.

analyzing the average spectra collected in the presence of an electroporating event (figure 5.4 c), three different temporal behaviors are visible; from $t = 0$ to $t = 600s$, before the electroporation has been induced, the signal is following the same behavior of the unperturbed samples. The detected molecules are the same as in the unperturbed samples, and the intensities are comparable. After the electroporation event, from $t = 600s$ to roughly $t = 1200s$, the average signal changes dramatically, showing the appearance of new peaks with a much higher intensity than the baseline, together with old peaks that increase their intensity while other disappear temporarily. The majority of changes happen in the Raman shift regions corresponding to proteins related peaks and lipid related molecular vibrations, suggesting that these molecules are involved in the rearrangement of the cell membrane. In fact, when the plasma membrane undergoes to a process of permeabilization, it follows a period of rearrangement of the lipids bilayer with the aid of several membrane proteins at the interface with the membrane [5], [86], [87].

The last 10 minutes (from 1200 sec to 1800 sec) of acquisition are characterized by a general decrease in the intensity of the peaks to a condition resembling the initial one and by the disappearance of some of the peaks that emerged after the electroporating event. The most convincing reason being the closure of the nanopores at the interface with the 3D nanoelectrode hot-spots, and the membrane reformation to the *pre-electroporation* conditions [19].

To test this hypothesis, the time evolution of single molecules has been studied through the evolution of their peaks. Before that however, a time average analysis has been performed to more clearly highlight the peaks that underwent to the most dramatic changes during the experiments.

5.1 Time evolution of single peaks

The analysis has been made on the average Raman signal showed in figure 5.4 c. Spectra have been divided in time bands and the average of the Raman signals over these intervals has been calculated. A time band called *PrePoration* represents the average spectrum of all the acquisitions that precede the electroporation event, from $t = 0\,sec$ to $t = 594\,sec$. The *PostPoration* signals, from $t = 612\,sec$ to $t = 1800\,sec$, have been divided in four time bands, each consisting of 5 consecutive minutes and the relatives averages have been calculated. The acquisitions between $594\,sec$ and $612\,sec$ have been discarded to avoid the influence of the electrical pulse train.

With the time-average analysis it has been possible to isolate the Raman peaks correlated to interesting molecular vibrations and studying their dynamic in time, in the attempt of explaining the plasma membrane behavior when perturbed with *in situ* electroporation.

The results are showed in figure 5.5, in which the five spectra represent the averages of the time-binned signals. From this analysis, some peaks result to have a stable intensity during the whole recording time, such as $954\,cm^{-1}$ assigned to cholesterol [62] and $975\,cm^{-1}$ related to fatty acid vibrational modes [81]. Their temporal evolution during the 30 minutes of experiments are showed in figure 5.6 a and b, and compared to the temporal behavior of the same molecules in the absence of the electroporation (spectra in black in the graphs). The electroporation moment is identified by a dotted line, after which the spectra present some broader oscillation respect to the not porated samples. However, the changes in intensity is at maximum of 1000 counts for both the detected molecules. Thus, their presence is constant overall the experiments, both in case of the electroporation and "at rest".

The behavior of these peaks suggests that the relative molecules are present in the enhancement area, close to the 3D plasmonic nanoelectrodes, during the

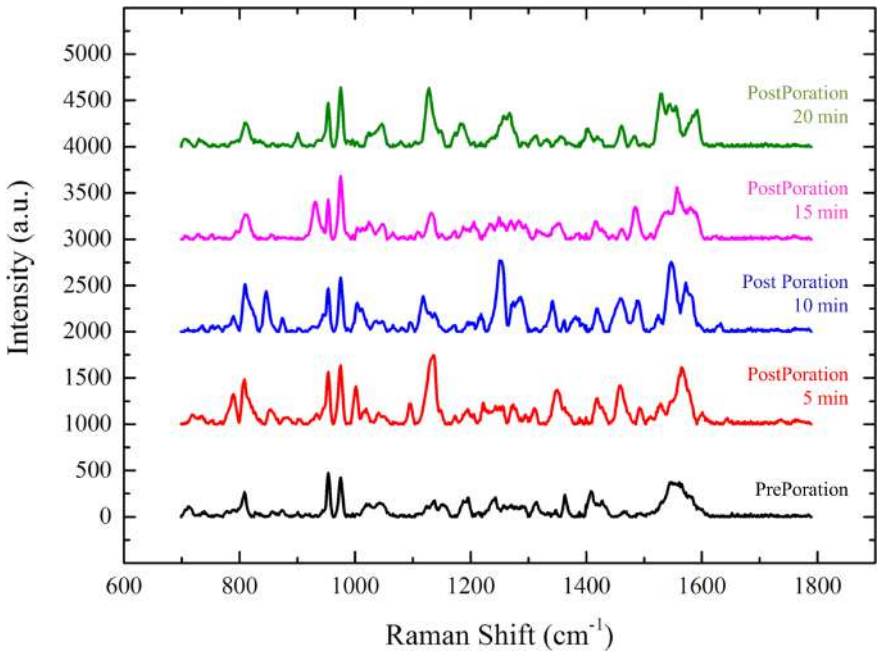

Figure 5.5: Time means of the averaged Raman signals. The black spectrum is the average of the *Preporation* signals, from $t = 0\,sec$ to $t = 594\,sec$. The others Raman spectra are the averages of different time slots after the electroporation, in particular the average of the Raman signals between $t = 612\,sec$ and $t = 900\,sec$ (red line), the average of the Raman spectra from $t = 900\,sec$ to $1200\,sec$ (blue spectrum), from $t = 1200\,sec$ and $1500\,sec$ (pink spectrum) and from $t = 1500\,sec$ to $t = 1800\,sec$ (green line).

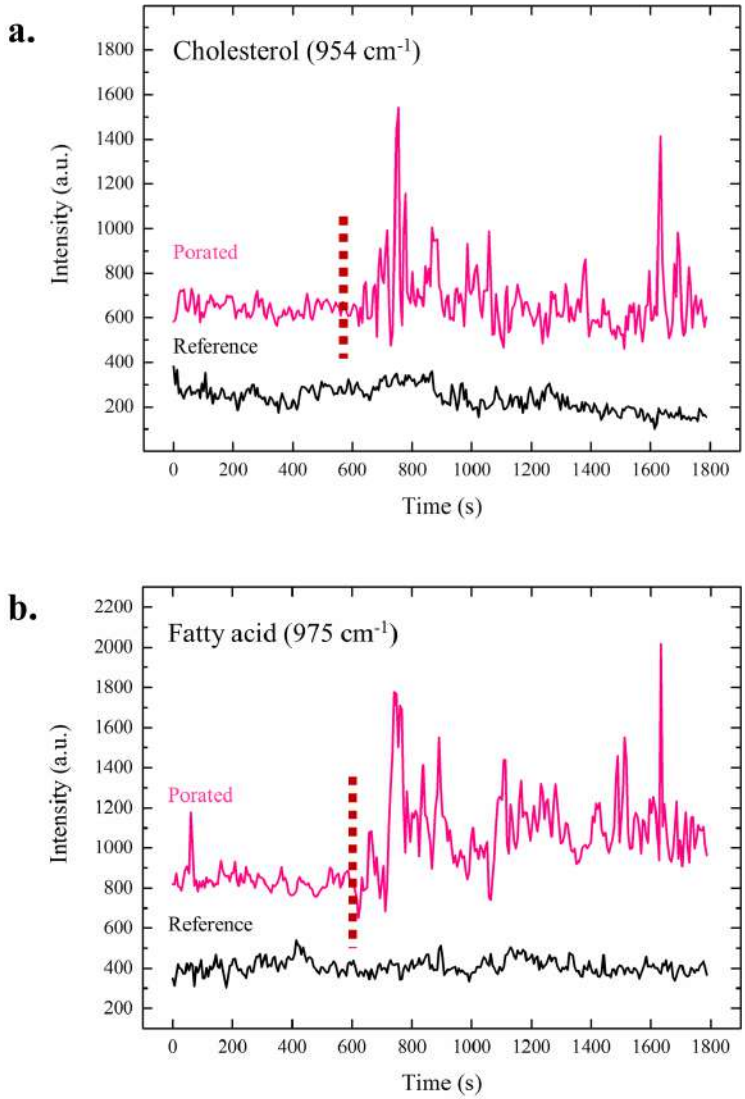

Figure 5.6: Temporal behavior of the a) cholesterol related peak at 954 cm^{-1} and b) fatty acid related peak at 975 cm^{-1} of the average spectrum both in the presence of the electroporation process (pink spectrum) and in the absence of it (black spectrum). The moment in which the electroporating pulse train has been applied is identified by the dotted line.

whole duration of the experiments.

Other molecules instead, exhibit their fingerprints only after the electroporation stimulus.

Lipid related peaks have been analyzed, including the $875\,cm^{-1}$ peak, assigned to the C - C stretching of phospholipids [81], the $1378\,cm^{-1}$ peak generically assigned to lipids [88], and the peak in $1464\,cm^{-1}$ related to CH_2 CH_3 deformations in cholesterol and triacylglycerols [89]. Their time behavior is showed in figure 5.7 a, b and c respectively.

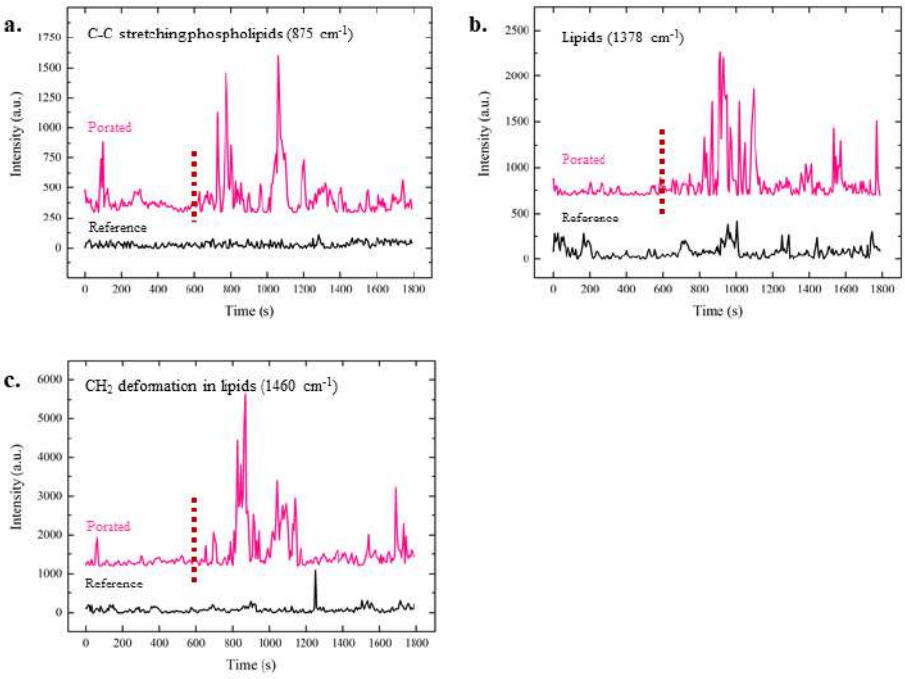

Figure 5.7: Time behavior of a) C - C stretching of phospholipids related peaks at $875\,cm^{-1}$, b) lipid related peak at $1378\,cm^{-1}$ and c) CH_2 CH_3 deformations of fatty acid and triacyglycerols vibrations ($1464\,cm^{-1}$) in the plasma membrane. In black the time behavior of the average lipid related peaks without the application of the electroporation. In pink the time evolution of the average peaks when electroporation has been performed at 600 sec (dotted line).

In each of the graph the time evolution of the peak in the absence of the electroporating event is depicted in black, while the dynamic of the molecular vibration when the electroporating pulse train has been applied is depicted in pink.

All the three peaks, and with them the relative molecules, present a dramatic increase in the intensity after the electroporation, suggesting a drastic change in their presence and orientation in the plasma membrane. It is interesting to notice how the oscillations are not synchronized, suggesting that each molecule has a specific role in the rearrangement of the membrane after the permeabilization in a certain temporal order. This lack of synchronization among the temporal evolution of different peaks together with the comparison with the samples without electroporation, are useful to confirm that the detected changes are not related to the measurement (laser power, environment conditions) but only to the electroporation event. Moreover, the molecules that are detected in the absence of electroporation, present changes in intensities comparable to those of the *pre-poration* time.

Time evolution of the protein vibrational modes have been studied (figure 5.8), in particular it has been investigate the dynamics of four peaks assigned to amino acids such as tyrosine, identified at $830\,cm^{-1}$ [88], the more intense one at $1002\,cm^{-1}$ related to the phenylalanine [90], the peak at $1211\,cm^{-1}$ assigned to both tyrosine and phenylalanine [88] and the one at $1552\,cm^{-1}$ assigned to tryptophan [88]. In addition, the dynamics of two peaks at $1302\,cm^{-1}$ and at $1545\,cm^{-1}$ assigned respectively to the $C-N$ stretching and $N-H$ bending vibration modes of the Amide III [82], [90] and to Amide II [91] have been studied.

Different behaviors have been noticed when electroporation was induced (purple lines in figure 5.8) in respect to measurements made without external stimulations (black spectra in figure 5.8).

In particular, the amino acids modes have a very stable and almost null

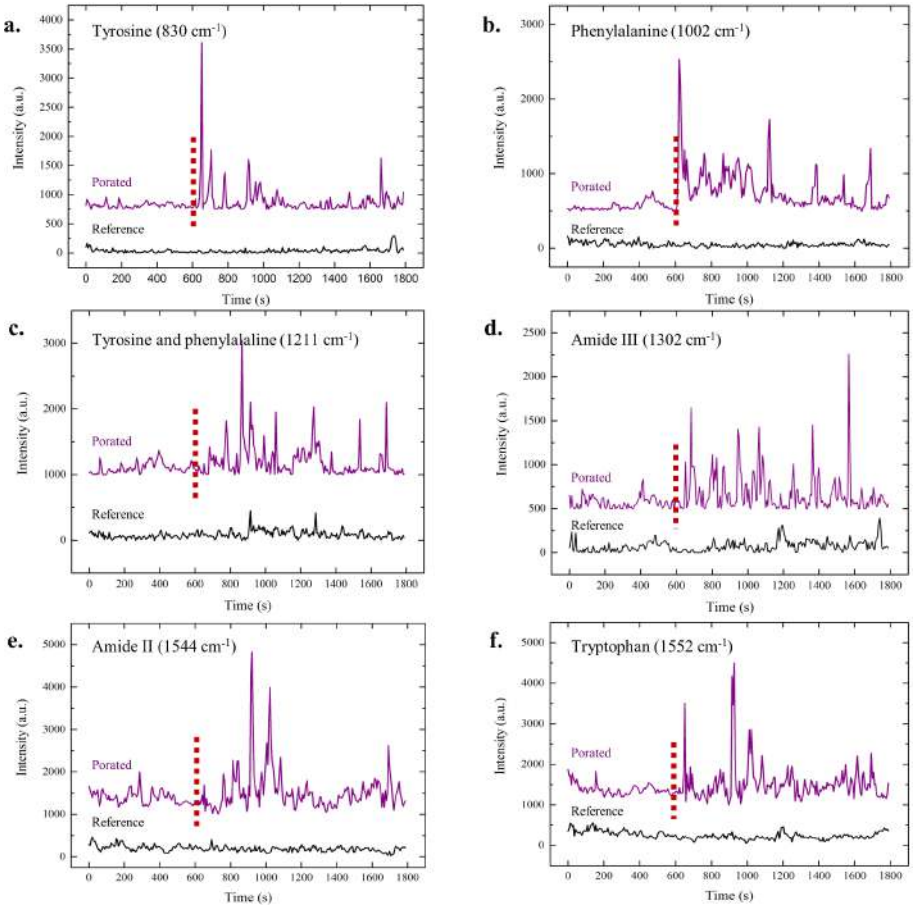

Figure 5.8: Time behavior of proteins related peaks when the system has been porated (purple spectra, electroporation indicated with the dotted line at 600 sec) and when the system has not been perturbed (black spectra). In particular, a) tyrosine related peak at $830\,cm^{-1}$, b) phenylalanine peak at $1002\,cm^{-1}$ and c) peak related to both tyrosine and phenylalanine at $1211\,cm^{-1}$. Then the vibrational modes related to d) amide III at $1302\,cm^{-1}$, e) amide II centered at $1545\,cm^{-1}$ and finally to f) tryptophan at $1552\,cm^{-1}$.

intensity in absence of the electroporation, while appeared after it with a very strong intensity. The amide II and amide III vibrational modes on the contrary, present some intense peaks also before the application of the electrical pulse train. However, also on them the effect of the plasma membrane permeabilization is visible. These dynamics, and in particular the amino acids vibrational modes, suggests the formation of hydrophilic nanopores on the plasma membrane that allowed cytoplasmic proteins to get closer to the 3D plasmonic nanoelectrode and led to the consequent detection of their enhanced Raman spectra.

Before the electroporation, the tyrosine, the phenylalanine and the tryptophan fingerprints are almost absent from the Raman spectra. Their peaks appear with a high intensity just after the electroporating pulse train and slowly decrease as the molecules move away from the 3D plasmonic nanoelectrodes after some time (5 minutes for the tyrosine). Also the amide II related peak shows a decrease in intensity after roughly 5 minutes from the electroporation, while the amide III vibrational mode persist until almost the end of the measurements (more than 15 minutes, see graph in figure 5.8 d).

The presence of hydrophilic nanopores on the plasma membrane can be induced in close proximity of the nuclear envelop. Looking to the cross section images, it is possible to imagine that nanopores can open also in the nuclear membrane (see inset in figure 4.4) when the nucleus is very close to the 3D plasmonic nanoelectrodes. In that scenario, DNA can exit from the safety of the nucleus and move close to the plasmonic enhancer, thus being detected from their vibrational modes. In this regard, temporal behavior of peaks assigned to DNA and nucleic acid have been analyzed with and without electroporation.

In figure 5.9, the peak at $790\,cm^{-1}$ has been assigned to O - P - O stretching modes related to DNA backbone [92] (figure 5.9 a), the vibrational modes at $1120\,cm^{-1}$ have been assigned to nucleic acid [88] (figure 5.9 b), the peak centered at $1252\,cm^{-1}$ has been assigned to the NH_2 vibrational modes of cytosine

and guanine [93] (figure 5.9 c), while the peak at $1573\,cm^{-1}$ has been assigned to guanine and adenine vibrational modes [58] (figure 5.9 d). The four Raman enhanced peaks showed a similar behavior among the experiments, with minimal changes in intensity, if the peaks were present, in absence of the electroporation and large intensities after the application of the electroporating pulse train. These results are very promising, suggesting the possibility of porating directly the nuclear envelop and gain access not only to cytoplasmic compartment, but also to the nuclear environment. Interestingly, protein related peaks and DNA related peaks behave differently; the nucleic acid and backbone vibrations in fact, appear after few minutes from the electroporation, while the peaks associated with protein vibrational modes present an increase in their intensity just after the electrical pulse train application.

In the attempt of shed some light on the rearrangement of the plasma membrane after and electroporating event, the peaks related to the α-glucose of glycoproteins [6], situated respectively at $847\,cm^{-1}$ (monosaccharides [94]) and $1343\,cm^{-1}$ (glucose [81]), have been analyzed. Glycoproteins are *transmembrane* proteins abundant in lipid rafts that exhibit abundant glucose and monosaccharides molecules in the extracellular domains. Understanding their recruitment after an electrical pulse train can help to prove the role of lipid raft and their proteins in helping exocytosis processes and the consequent sealing of the membrane nanopores [87].

The effects of electroporation are visible at 600 seconds when the peak signals appear and start to oscillate in time (see figure 5.10 a, b). Monosaccharides reach a peak in their presence after roughly 5 minutes (1200 sec) from the electroporation event, dropping their intensity radically as if their role has been performed and the molecules can scatter again in the plasma membrane, far from the permeabilized region.

The biological phenomena involved in the nanopores closure are still a matter of debate. Recently, it has been demonstrated that endosomal sorting

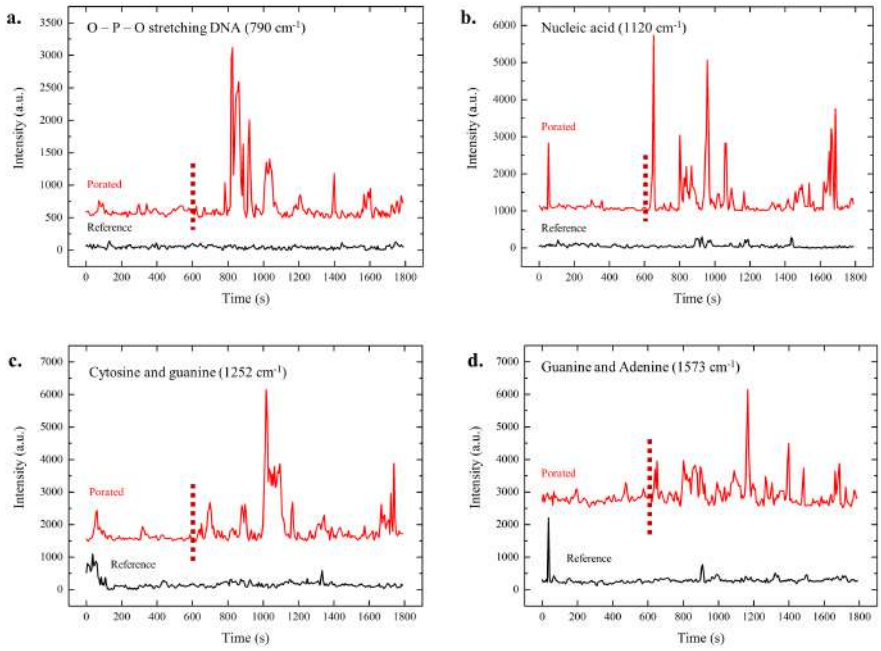

Figure 5.9: Dynamic behavior in time of DNA and nucleic acid associated peaks. a) 790 cm^{-1} peak associated to O - P - O stretching of DNA, b) vibrational mode assigned to nucleic acid at 1120 cm^{-1}, c) peak centered at 1252 cm^{-1} associated to vibration of cytosine and guanine, and d) peak at 1573 cm^{-1} related to guanine and adenine vibrational modes. Red spectra are the average of electroporated samples at 600 sec (dotted line), while black spectra are the reference, to which electroporation have not been applied.

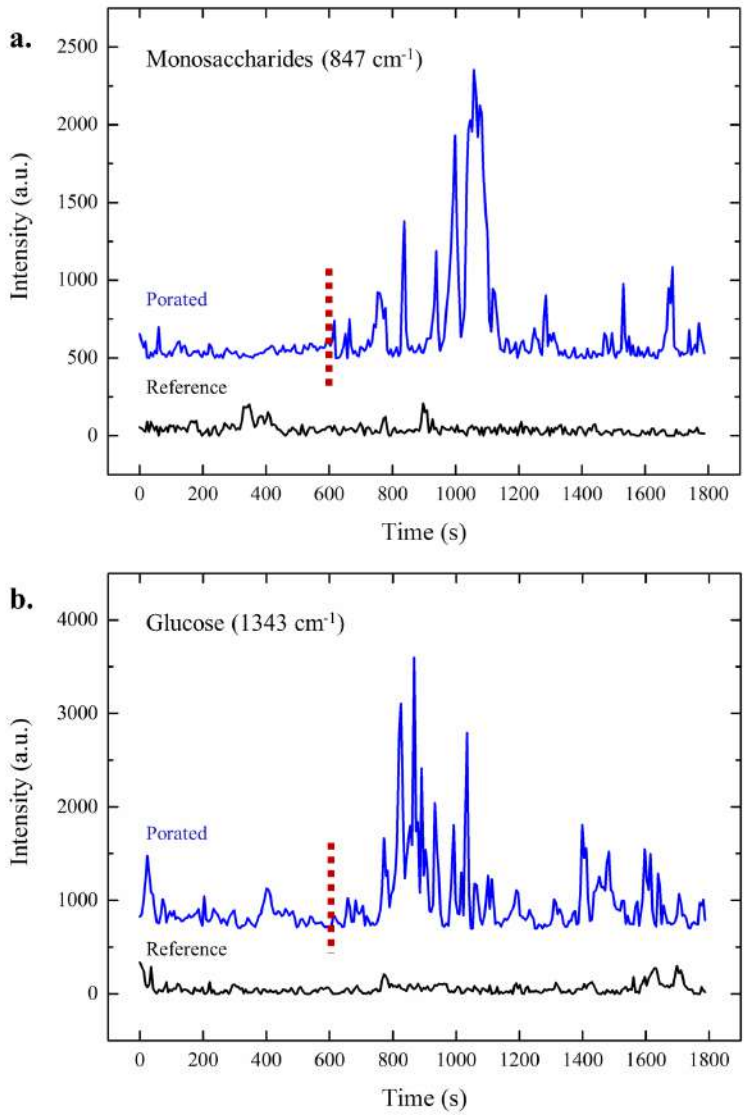

Figure 5.10: Time-resolved dynamics of a) monosaccharides peak at 847 cm^{-1} and b) glucose peak at 1343 cm^{-1}. With electroporation (blue) and without electroporation (black). The dotted line represents the moment in which the electroporating pulse train have been applied.

complexes required for transport (ESCRT) are key players in the reforming of cellular membranes [5]. In particular, these machines allow endosomes to bind and fuse with plasma membrane. Endosomes are intracellular compartments responsible for the transport of molecules and vesicles to and from the Golgi apparatus. When endosomes merge with the plasma membrane releasing their content into the extracellular space, they are called exosomes [95]. Studies have been made on the vibrational modes of exosomes isolated from cell cultures with different methods, to remove bias due to the used technique [88]. Lee et al. in particular, analyzed the Raman enhanced spectrum of exosomes extracted form cells by a total exosome isolation reagent (TEIR) and confronted the detected peaks with those excited when the isolation has been made by ultra-centrifugation; in this way, different sizes and conformations of exosomes have been characterized by their Raman fingerprints.

Several vibrational modes assigned to ESCRT have been already analyzed in this thesis, such the peaks at $830\,cm^{-1}$ (tyrosine), $1002\,cm^{-1}$ (phenylalanine), $1120\,cm^{-1}$ (nucleic acid), $1211\,cm^{-1}$ (tyrosine and phenylalanine), $1303\,cm^{-1}$ (amide III), $1378\,cm^{-1}$ (lipids), $1552\,cm^{-1}$ (tryptophan), and each of them showed an interesting behavior in time after the electroporation. In addition, also the vibrational mode at $1394\,cm^{-1}$ related to the CH_2 rocking [88], that is a change in angle between two hydrogens and the rest of the molecule in the carbon plane, that has been identified as one of the fingerprints of the exosomes, shows a dynamics similar to other molecules (see figure 5.11). These results point in the direction of the presence of exosomes *in situ* where electroporation has been performed. Such finding would give new strength to the theory of ESCRT as important players in the healing of the plasma membrane after its permeabilization, helping exosomes to merge with the broken lipid bilayer in the attempt of healing it.

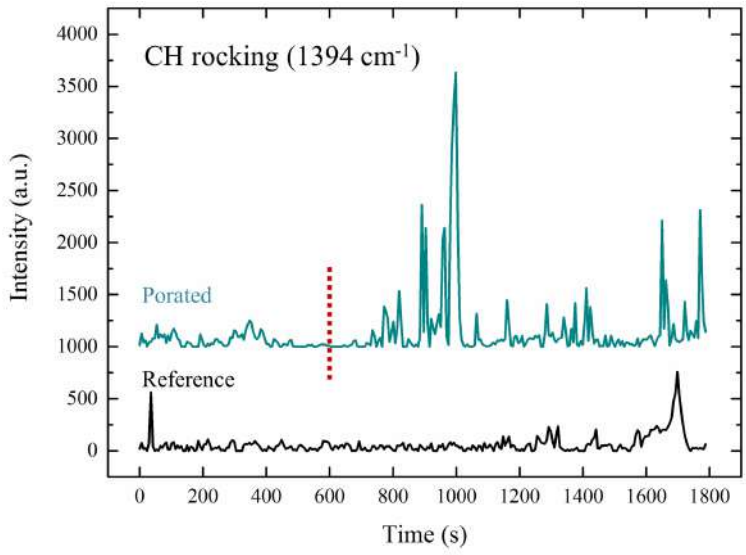

Figure 5.11: Time evolution of CH rocking related Raman peak at $1394\,cm^{-1}$ in presence (cyan) and in absence (black) of electroporation (at 600 sec, in correspondence of the dotted line).

Chapter 6

Conclusion

Interfacing biological samples and nanostructured surfaces finds applications in countless fields such as tissue engineering [36], electrophysiology over large cell cultures [96], *in vitro* and *in vivo* delivery of molecules and nanoparticles [7], intracellular sampling [26] and spectroscopic analysis of biological specimens [62]. The outcomes have impact both on basic research and in medicine.

This work is based on a recently developed 3D nanostructured device [80] that has been previously exploited to address the extra and intra - cellular environment in multiple applications such Raman spectroscopy [62], optoporation and delivery of molecules [10] and electrical recordings of action potentials [24]. Throughout the results and developments achieved and described in this thesis, the performance and the capabilities of the 3D hollow nanostructures have been extended to new biological application fields, further deepening our understanding of the cell-nanostructure interface.

The purpose of this thesis has been twofold. Firstly, a novel microfluidic bio-device and an optimized electroporation protocol have been realized and refined exploiting the recent developments on 3D hollow nanostructures. Subsequently, the behavior of the cellular membrane in contact with 3D nanostructures has been explored by means of SERS spectroscopy and FIB/SEM

imaging, revealing new aspects of the membrane dynamics under specific external stimuli and in resting conditions.

The device developed in the first part of the PhD work is made of 3D hollow, plasmonic and electrically conductive nanostructures arrays protruding from a flat substrate. The contribution discussed in the present research involves the implementation of an electroporation protocol to open nanopores on the cell membrane applying a short pulse train, and to deliver molecules in the targeted cells through the inner nanochannel of the 3D nanostructures. To achieve this result, possible optimizations of a passivation layer on the flat substrate have been explored. The final outcome has led to a *soft-electroporation* protocol in which the electric pulse train is applied only through the nanometer tip of the 3D nanoelectrodes, and the permeabilization of the cell membrane is achieved with a low applied voltage (*soft-electroporation*), thus reducing the formation of toxic reactive oxygen species. The permeabilization of the plasma membrane in correspondence of the 3D hollow nanoelectrode tip has been exploited to intracellularly deliver fluorescent molecules in the targeted cells from a separated microfluidic compartment. This result represents an important development in respect to the state of the art because it allows for the reproducible intracellular delivery in mild and non-invasive conditions.

The interface between *in vitro* cell systems and the 3D substrate has been investigated by means of FIB cross sectioning and SEM imaging. The results are in accordance with several studies on 3D nanostructured substrates [50], [72], showing a tight adhesion between the cell membrane and the substrate, in particular where 3D features are present, and the absence of spontaneous internalization of the 3D nanostructures. Different behaviors of the plasma membrane and the nuclear envelop have been showed when close to the 3D nanostructures. Cellular membrane exhibited a tight sealing firmly wrapping the 3D nanostructure along the totality of its length, while the nuclear envelop presented only local bending close to the 3D nanostructures, trying to preserve

the spherical-ish shape that distinguishes the nucleus.

In the second part of this PhD work, the device has been revisited to make the 3D nanostructures plasmonically resonant at a specific wavelength and removing its nanofluidic capabilities. Taking advantage of the plasmonic properties of the 3D nanostructures, the device has been exploited to study the *in situ* dynamics of the cell membrane when nanopores have been generated by an electrical pulse train. Laser light is able to couple with the nanostructures when the 3D geometry has been properly tuned, and the electric field results to be locally enhanced in specific hot-spots along the 3D nanoelectrode. The localized field enhancement allowed to record specific radiation, such as Raman spectra, otherwise too weak to be detected in respect to more intense signals like the fluorescence emitted by the system. Since the Raman signal encodes for the biochemical molecules present in the plasma membrane, the changes in the spectra have been directly related to molecular changes in the orientation and composition of the investigated region. The experiments performed in this thesis represent a novel approach to observe in real time and with high resolution the molecular dynamics of the cell membrane subjected to external stimuli. Moreover, the results presented in this work are also in accordance with data in literature and show an average closure time of the nanopores in the order of 10 minutes after the electroporation [17], [18]. The molecular changes due to electroporation have been investigated for 20 minutes, the behavior of several molecules tightened to the plasma membrane rearrangement has been studied and the results have been compared to the same measurements when electroporation has not been induced.

Several molecules have been identified within the recorded Raman enhanced peaks, and the technique resulted promising in unveiling the mechanisms behind the self-healing of the plasma membrane after the aperture of nanopores by an electrical pulse train. The results agreed with the hypothesis of exosomes merging with the plasma membrane to close nanopores, thus supporting the

involvement of ESCRT machine in the repair mechanism of the cell membrane.

Finally, the presence of very intense vibrational modes related to DNA and nucleic acid after *in situ* electroporation hints to the possibility of directly access the nuclear compartment.

This work is the first study on the electroporation dynamics performed by SERS and it is located in a landscape of increasing interest from the scientific community on the interaction between nanostructures and cells and their interface.

Publications and Contributions

1. V. Caprettini, J. Huang, F. Moia, A. Jacassi, C. A. Gonano, M. Dipalo, F. De Angelis "Cell membrane dynamics: a 3D plasmonic approach to study changes in the cellular Raman signals at rest and during electroporation" **in preparation**

2. M. Dipalo, G. Melle, L. Lovato, A. Jacassi, F. Santoro, V. Caprettini, A. Schirato, A. Alabastri, D. Garoli, F. Tantussi, F. De Angelis "Intracellular Recordings on High-Density CMOS-MEAs by Plasmonic Meta-Electrodes" **submitted**

3. J.A. Huang, V. Caprettini, Y. Zhao, G. Melle, N. Maccaferri, M. Ardini, F. Tantussi, M. Dipalo, F. De Angelis "Controlled Intracellular Delivery of Single Particles in Single Cells by 3D Hollow Nanoelectrodes" **submitted**

4. R. Capozza, C. A. Gonano, V. Caprettini, F. Santoro, F. De Angelis "Molecular Dynamics model of cell membrane disruption by vertical nanopillars: the role of curvature and traction forces" **under revision**

5. V. Caprettini, A. Cerea, G. Melle, L. Lovato, R. Capozza, J. Huang, F. Tantussi, M. Dipalo, F. De Angelis "Soft electroporation for deliver-

ing molecules into tightly adherent mammalian cells through 3D hollow nanoelectrodes" **Sci. Rep.** 7, 8524, 2017

6. A. Cerea, V. Caprettini, G. Melle, G. Bruno, M. Leoncini, A. Barbaglia, F. Santoro, M. Dipalo "Coaxial-like three-dimensional nanoelectrodes for biological applications" **Microelectron. Eng.**, 2017

7. M. Dipalo, H. Amin, L. Lovato, F. Moia, V. Caprettini, G. C. Messina, F. Tantussi, L. Berdondini, F. De Angelis "Intracellular and extracellular recording of spontaneous action potentials in mammalian neurons and cardiac cells with 3D plasmonic nano-electrodes" **Nano Letters** 17 (6), 3932 - 3939, 2017

8. A. Cerea, D. Garoli, P. Zilio, M. Dipalo, E. Calandrini, A. Jacassi, V. Caprettini, A. Carrara, M. G. Pelizzo, F. De Angelis "Modified three-dimensional nanoantennas for infrared hydrogen detection" **Microelectron. Eng.**, 102, 105-109, 2016

9. M. Dipalo, F. Tantussi, V. Caprettini, A. Jacassi, V. Shalabaeva, A. Cerea, S. Perotto, F. De Angelis "Mimicking and interfacing neurobiological architectures with nanostructured materials" **IEEE 10th International Congress on Advanced Electromagnetic Materials in Microwaves and Optics (METAMATERIALS)**, 2016

10. V. Caprettini, G.C. Messina, M. Dipalo, R. La Rocca, A. Cerea, F. De Angelis "SERS spectroscopy, electrical recording and intracellular injection in neuronal networks with 3D plasmonic nanoantennas" **Proc. of SPIE**, 9740, 2016

11. V. Caprettini, M. Dipalo, G. C. Messina, L. Lovato, F. Tantussi, F. De Angelis "3D Plasmonic nanostructures for in-vitro applications in neu-

roscience and cell biology" **IEEE-NANO, 2016 IEEE 16th International Conference on Nanotechnology**, 491-493, 2016

12. G. C. Messina, M. Dipalo, R. La Rocca, P. Zilio, V. Caprettini, R. Proietti Zaccaria, A. Toma, F. Tantussi, L. Berdondini, F. De Angelis "Spatially, Temporally, and Quantitatively Controlled Delivery of Broad Range of Molecules into Selected Cells through Plasmonic Nanotubes" **Advanced Materials**, 27, 44, 7145-7149, 2015

Conferences

1. "SERS study of celular membrane dynamics on 3D plasmonic nanoelectrodes during electroporation" *Poster presentation* **MNE 2017**, Braga, Portugal, September 2017

2. "Cell electroporation and intracellular delivery by mean of 3D vertical hollow nanoelectrodes" *Talk presentation* **NANO 2017 - IEEE-Xplore**, Pittsburgh, PA, USA, July 2017

3. "Localized Plasmonic Nanobubbles: Mechanism and Application" *Poster presentation.* **Plasmonica**, Padua, Italy, June 2015

Bibliography

[1] Kai Simons and Winchil L.C. Vaz. Model Systems, Lipid Rafts, and Cell Membranes. *Annual Review of Biophysics and Biomolecular Structure*, 33(1):269–295, 2004.

[2] Lawrence Rajendran and Kai Simons. Lipid rafts and membrane dynamics. *Journal of cell science*, 118:1099–1102, 2005.

[3] Erdinc Sezgin, Ilya Levental, Satyajit Mayor, and Christian Eggeling. The mystery of membrane organization: composition, regulation and roles of lipid rafts. *Nature Reviews Molecular Cell Biology*, 18(6):361–374, 2017.

[4] D. Lingwood and K. Simons. Lipid Rafts As a Membrane-Organizing Principle. *Science*, 327(5961):46–50, 2010.

[5] A. J. Jimenez, P. Maiuri, J. Lafaurie-Janvore, S. Divoux, M. Piel, and F. Perez. ESCRT Machinery Is Required for Plasma Membrane Repair. *Science*, 343(6174):1247136–1247136, 2014.

[6] David L Nelson and Michael M Cox. *Lehninger Principles of Biochemistry*. 2004.

[7] Martin P Stewart, Armon Sharei, Xiaoyun Ding, Gaurav Sahay, Robert Langer, and Klavs F Jensen. Break and enter: in vitro and ex vivo strategies for intracellular delivery. *Nature*, 538(7624):183–192, 2016.

[8] Francesca Bugli, Valeria Caprettini, Margherita Cacaci, Cecilia Martini, Francesco Paroni Sterbini, Riccardo Torelli, Stefano Della Longa, Massimiliano Papi, Valentina Palmieri, Bruno Giardina, Brunella Posteraro, Maurizio Sanguinetti, and Alessandro Arcovito. Synthesis and characterization of different immunogenic viral nanoconstructs from rotavirus VP6 inner capsid protein. *International Journal of Nanomedicine*, 9(1):2727–2739, 2014.

[9] Qihui Fan, Wenqi Hu, and Aaron T. Ohta. Efficient single-cell poration by microsecond laser pulses. *Lab Chip*, 15(2):581–588, 2015.

[10] Gabriele C. Messina, Michele Dipalo, Rosanna La Rocca, Pierfrancesco Zilio, Valeria Caprettini, Remo Proietti Zaccaria, Andrea Toma, Francesco Tantussi, Luca Berdondini, and Francesco De Angelis. Spatially, Temporally, and Quantitatively Controlled Delivery of Broad Range of Molecules into Selected Cells through Plasmonic Nanotubes. *Advanced Materials*, 27(44):7145–7149, 2015.

[11] Mario R. Capecchi. High efficiency transformation by direct microinjection of DNA into cultured mammalian cells. *Cell*, 22(2):479–488, 1980.

[12] Fong Kuan Wong, Christiane Haffner, Wieland B. Huttner, and Elena Taverna. Microinjection of membrane-impermeable molecules into single neural stem cells in brain tissue. *Nature Protocols*, 9(5):1170–1182, 2014.

[13] Sangpil Yoon, Min Gon Kim, Chi Tat Chiu, Jae Youn Hwang, Hyung Ham Kim, Yingxiao Wang, and K Kirk Shung. Direct and sustained intracellular delivery of exogenous molecules using acoustic-transfection with high frequency ultrasound. *Scientific reports*, 6:20477, feb 2016.

[14] Chong Xie, Ziliang Lin, Lindsey Hanson, Yi Cui, and Bianxiao Cui. Intracellular recording of action potentials by nanopillar electroporation. *Nature Nanotechnology*, 7(3):185–190, 2012.

[15] Valeria Caprettini, Andrea Cerea, Giovanni Melle, Laura Lovato, Rosario Capozza, Jian-An Huang, Francesco Tantussi, Michele Dipalo, and Francesco De Angelis. Soft electroporation for delivering molecules into tightly adherent mammalian cells through 3D hollow nanoelectrodes. *Scientific Reports*, 7(1):8524, 2017.

[16] C. Chen, S. W. Smye, M. P. Robinson, and J. A. Evans. Membrane electroporation theories: A review. *Medical and Biological Engineering and Computing*, 44(1-2):5–14, 2006.

[17] Aviad Hai and Micha E. Spira. On-chip electroporation, membrane repair dynamics and transient in-cell recordings by arrays of gold mushroom-shaped microelectrodes. *Lab on a Chip*, 12(16):2865–2873, 2012.

[18] Bruno Gabriel and Justin Teissié. Control by electrical parameters of short- and long-term cell death resulting from electropermeabilization of Chinese hamster ovary cells. *BBA - Biochimica et Biophysica Acta*, 1266:171–178, 1995.

[19] G. Saulis, M. S. Venslauskas, and J. Naktinis. Kinetics of pore resealing in cell-membranes after electroporation. *Bioelectrochemistry and Bioenergetics*, 26(1):1–13, 1991.

[20] R. P. Joshi and K. H. Schoenbach. Electroporation dynamics in biological cells subjected to ultrafast electrical pulses: A numerical simulation study. *Physical Review E - Statistical Physics, Plasmas, Fluids, and Related Interdisciplinary Topics*, 62(1 B):1025–1033, 2000.

[21] Huntington Potter, Lawrence Weir, and Philip Leder. Enhancer-dependent expression of human Kc immunoglobulin genes introduced into mouse pre-B lymphocytes by electroporation. 81(November):7161–7165, 1984.

[22] Tao Geng and Chang Lu. Microfluidic electroporation for cellular analysis and delivery. *Lab on a chip*, 13(19):3803–21, 2013.

[23] Wonmo Kang, Fazel Yavari, Majid Minary-Jolandan, Juan P Giraldo-Vela, Asmahan Safi, Rebecca L McNaughton, Victor Parpoil, and Horacio D Espinosa. Nanofountain probe electroporation (NFP-E) of single cells. *Nano letters*, 13(6):2448–57, 2013.

[24] Michele Dipalo, Hayder Amin, Laura Lovato, Fabio Moia, Valeria Caprettini, Gabriele C Messina, Francesco Tantussi, Luca Berdondini, and Francesco De Angelis. Intracellular and Extracellular Recording of Spontaneous Action Potentials in Mammalian Neurons and Cardiac Cells with 3D Plasmonic Nanoelectrodes. *Nano letters*, 2017.

[25] Xi Xie, Alexander M Xu, Matthew R Angle, Noureddine Tayebi, Piyush Verma, and Nicholas A Melosh. Mechanical model of vertical nanowire cell penetration. *Nano letters*, 13(12):6002–8, jan 2013.

[26] Yuhong Cao, Martin Hjort, Haodong Chen, Fikri Birey, Sergio A. Leal-Ortiz, Crystal M. Han, Juan G. Santiago, Sergiu P. Pasca, Joseph C. Wu, and Nicholas A. Melosh. Nondestructive nanostraw intracellular sampling for longitudinal cell monitoring. *Proceedings of the National Academy of Sciences*, 114(10):E1866–E1874, 2017.

[27] Bruno Gabriel and Justin Teissié. Generation of reactive - oxygen species induced by electropermeabilization of Chinese hamster ovary cells and

their consequence on cell viability. *European Journal of Biochemistry*, 223(1):25–33, 1994.

[28] Rodney L. LeRoy. The Thermodynamics of Aqueous Water Electrolysis. *Journal of The Electrochemical Society*, 127(9):1954, 1980.

[29] M S Wrighton, D S Ginley, P T Wolczanski, a B Ellis, D L Morse, and a Linz. Photoassisted electrolysis of water by irradiation of a titanium dioxide electrode. *Proceedings of the National Academy of Sciences of the United States of America*, 72(4):1518–1522, 1975.

[30] Pouyan E Boukany, Yun Wu, Xi Zhao, Kwang J Kwak, Piotr J Glazer, Kam Leong, and L James Lee. Nonendocytic Delivery of Lipoplex Nanoparticles into Living Cells Using Nanochannel Electroporation. *Advanced healthcare materials*, 3:682–689, 2014.

[31] Bryan C Dickinson and Christopher J Chang. Chemistry and biology of reactive oxygen species in signaling or stress responses. *Nature Chemical Biology*, 7(8):504–511, 2011.

[32] Pouyan E. Boukany, Andrew Morss, Wei-ching Liao, Brian Henslee, HyunChul Jung, Xulang Zhang, Bo Yu, Xinmei Wang, Yun Wu, Lei Li, Keliang Gao, Xin Hu, Xi Zhao, O. Hemminger, Wu Lu, Gregory P. Lafyatis, and L. James Lee. Nanochannel electroporation delivers precise amounts of biomolecules into living cells. *Nature Nanotechnology*, 6(11):747–754, 2011.

[33] Anqi Zhang and Charles M. Lieber. Nano-Bioelectronics. *Chemical Reviews*, 116(1):215–257, 2016.

[34] Furqan Ali Shah, Bengt Nilson, Rickard Brånemark, Peter Thomsen, and Anders Palmquist. The bone-implant interface - nanoscale analysis of clin-

ically retrieved dental implants. *Nanomedicine: Nanotechnology, Biology and Medicine*, 10(8):1729–1737, nov 2014.

[35] Robert Langer and David A. Tirrell. Designing materials for biology and medicine. *Nature*, 428(6982):487–492, 2004.

[36] Molly M Stevens and Julian H George. Exploring and engineering the cell surface interface. *Science (New York, N.Y.)*, 310(November):1135–1138, 2005.

[37] Anthony C. Jones, Christoph H. Arns, Adrian P. Sheppard, Dietmar W. Hutmacher, Bruce K. Milthorpe, and Mark A. Knackstedt. Assessment of bone ingrowth into porous biomaterials using MICRO-CT. *Biomaterials*, 28(15):2491–2504, may 2007.

[38] Francesco Gentile, Luca Tirinato, Edmondo Battista, Filippo Causa, Carlo Liberale, Enzo M. di Fabrizio, and Paolo Decuzzi. Cells preferentially grow on rough substrates. *Biomaterials*, 31(28):7205–7212, 2010.

[39] Thomas P Kraehenbuehl, Robert Langer, and Lino S Ferreira. Three-dimensional biomaterials for the study of human pluripotent stem cells. *Nature methods*, 8(9):731–736, 2011.

[40] Dylan M. Owen, Astrid Magenau, David Williamson, and Katharina Gaus. The lipid raft hypothesis revisited - new insights on raft composition and function from super-resolution fluorescence microscopy. *BioEssays*, 34(9):739–747, 2012.

[41] Jeff W Lichtman and José-Angel Conchello. Fluorescence microscopy. *Nature Methods*, 2(12):910–919, 2005.

[42] Wenting Zhao, Lindsey Hanson, Hsin-Ya Lou, Matthew Akamatsu, Praveen D. Chowdary, Francesca Santoro, Jessica R. Marks, Alexandre

Grassart, David G. Drubin, Yi Cui, and Bianxiao Cui. Nanoscale manipulation of membrane curvature for probing endocytosis in live cells. *Nature Nanotechnology*, (June):1–9, 2017.

[43] Juan C. Tapia, Narayanan Kasthuri, Kenneth Hayworth, Richard Schalek, Jeff W. Lichtman, Stephen J Smith, and Joann Buchanan. High contrast en bloc staining of neuronal tissue for field Emission Scanning Electron Microscopy. *Nature protocols*, 7(2):193–206, 2013.

[44] Brent Fultz and James M. Howe. *Transmission Electron Microscopy and Diffractometry of Materials*. Springer, 4 edition, 2013.

[45] Ludwig Reimer and Helmut Kohl. *Transmission Electron Microscopy; Physics of Image Formation*. Springer, 5 edition, 2008.

[46] M. Baram and W. D. Kaplan. Quantitative HRTEM analysis of FIB prepared specimens. *Journal of Microscopy*, 232(3):395–405, 2008.

[47] Juliana C Araujo, Francisco C Téran, Roberto A Oliveira, Edson A A Nour, Martha A P Montenegro, José R Campos, and Rosana F Vazoller. Comparison of hexamethyldisilazane and critical point drying treatments for SEM analysis of anaerobic biofilms and granular sludge. *Journal of Electron Microscopy*, 52(4):429–433, sep 2003.

[48] A M Glauert and P R Lewis. *Biological Specimen Preparation for Transmission Electron Microscopy*. Princeton Legacy Library. Princeton University Press, 2014.

[49] Andrea Friedmann, Andreas Hoess, Andreas Cismak, and Andreas Heilmann. Investigation of cell-substrate interactions by focused ion beam preparation and scanning electron microscopy. *Acta Biomaterialia*, 7(6):2499–2507, 2011.

[50] C. Chiappini, E. De Rosa, J. O. Martinez, X. Liu, J. Steele, M. M. Stevens, and E. Tasciotti. Biodegradable silicon nanoneedles delivering nucleic acids intracellularly induce localized in vivo neovascularization. *Nature Materials*, 14(5):532–539, 2015.

[51] A. Belu, J. Schnitker, S. Bertazzo, E. Neumann, D. Mayer, A. OffenhÄusser, and F. Santoro. Ultra-thin resin embedding method for scanning electron microscopy of individual cells on high and low aspect ratio 3D nanostructures. *Journal of Microscopy*, 263(1):78–86, 2016.

[52] Michael J. Rust, Mark Bates, and Xiaowei Zhuang. Sub-diffraction-limit imaging by stochastic optical reconstruction microscopy (STORM). *Nature Methods*, 3(10):793–795, 2006.

[53] K König. Multiphoton microscopy in life sciences. *Journal of microscopy*, 200(Pt 2):83–104, 2000.

[54] Warren R. Zipfel, Rebecca M. Williams, and Watt W. Webb. Nonlinear magic: Multiphoton microscopy in the biosciences. *Nature Biotechnology*, 21(11):1369–1377, 2003.

[55] Katrin I. Willig, Benjamin Harke, Rebecca Medda, and Stefan W. Hell. STED microscopy with continuous wave beams. *Nature Methods*, 4(11):915–918, 2007.

[56] Aaron M. Streets, Ang Li, Tao Chen, and Yanyi Huang. Imaging without fluorescence: Nonlinear optical microscopy for quantitative cellular imaging. *Analytical Chemistry*, 86(17):8506–8513, 2014.

[57] Ioan Notingher. Raman Spectroscopy Cell-based Biosensors. *Sensors*, 7(8):1343–1358, jul 2007.

[58] Nicholas Stone, Catherine Kendall, Jenny Smith, Paul Crow, and Hugh Barr. Raman spectroscopy for identification of epithelial cancers. *Faraday Discussions*, 126:141, 2004.

[59] Martin Hedegaard, Christian Matthäus, Søren Hassing, Christoph Krafft, Max Diem, and Jürgen Popp. Spectral unmixing and clustering algorithms for assessment of single cells by Raman microscopic imaging. *Theoretical Chemistry Accounts*, 130(4-6):1249–1260, 2011.

[60] Katrin Kneipp. Surface-enhanced raman scattering. *Physics Today*, 60(11):40–46, 2007.

[61] G. V. Pavan Kumar. Plasmonic nano-architectures for surface enhanced Raman scattering: a review. *Journal of Nanophotonics*, 6(1):064503, 2012.

[62] Rosanna La Rocca, Gabriele C. Messina, Michele Dipalo, Victoria Shalabaeva, and Francesco De Angelis. Out-of-Plane Plasmonic Antennas for Raman Analysis in Living Cells. *Small*, 11(36):4632–4637, 2015.

[63] Stefan a Maier. *Plasmonics : Fundamentals and Applications*, volume 677. 2004.

[64] Eric Le Ru and Pablo Etchegoin. *Principles of Surface-Enhanced Raman Spectroscopy: and related plasmonic effects*. Elsevier, first edit edition, 2008.

[65] Gabriele C Messina, Mario Malerba, Pierfrancesco Zilio, Ermanno Miele, Michele Dipalo, Lorenzo Ferrara, and Francesco De Angelis. Hollow plasmonic antennas for broadband SERS spectroscopy. *Beilstein. Journal of Nanotechnology*, 6:492–498, 2015.

[66] Gang Lu, Herlinde De Keersmaecker, Liang Su, Bart Kenens, Susana Rocha, Eduard Fron, Chang Chen, Pol Van Dorpe, Hideaki Mizuno, Johan

Hofkens, James A Hutchison, and Hiroshi Uji-i. Live-cell SERS endoscopy using plasmonic nanowire waveguides. *Advanced Materials*, 26(30):5124–8, aug 2014.

[67] Francesco De Angelis, Mario Malerba, Maddalena Patrini, Ermanno Miele, Gobind Das, Andrea Toma, Remo Proietti Zaccaria, and Enzo Di Fabrizio. 3D hollow nanostructures as building blocks for multifunctional plasmonics. *Nano Letters*, 13(8):3553–3558, 2013.

[68] Michele Dipalo, Gabriele C Messina, Hayder Amin, Rosanna La Rocca, Victoria Shalabaeva, Alessandro Simi, Alessandro Maccione, Pierfrancesco Zilio, Luca Berdondini, and Francesco De Angelis. 3D plasmonic nanoantennas integrated with MEA biosensors. *Nanoscale*, 7:3703–3711, 2015.

[69] R. Larsson, G. Selén, H. Björklund, and P. Fagerholm. Intraocular PMMA lenses modified with surface-immobilized heparin: evaluation of biocompatibility in vitro and in vivo. *Biomaterials*, 10(8):511–516, 1989.

[70] Jaehwan Ahn, Sang Jun Son, and Junhong Min. The control of cell adhesion on a PMMA polymer surface consisting of nanopillar arrays. *Journal of Biotechnology*, 164(4):543–548, 2013.

[71] N. N. Greenwood and A. Earnshaw. *Chemistry of the elements*. Pergamon Press, 1984.

[72] Francesca Santoro, Wenting Zhao, Lydia-Marie Joubert, Liting Duan, Jan Schnitker, Yoeri van de Burgt, Hsin-Ya Lou, Bofei Liu, Alberto Salleo, Lifeng Cui, Yi Cui, and Bianxiao Cui. Revealing the Cell–Material Interface with Nanometer Resolution by Focused Ion Beam/Scanning Electron Microscopy. *ACS Nano*, 11:8320 – 8328, 2017.

[73] S. J. Randolph, J. D. Fowlkes, and P. D. Rack. Focused, nanoscale electron-beam-induced deposition and etching. *Critical Reviews in Solid State and Materials Sciences*, 31(3):55–89, 2006.

[74] Henrik Persson, Carsten Købler, Kristian Mølhave, Lars Samuelson, Jonas O. Tegenfeldt, Stina Oredsson, and Christelle N. Prinz. Fibroblasts cultured on nanowires exhibit low motility, impaired cell division, and DNA damage. *Small*, 9(23):4006–4016, 2013.

[75] Christelle N Prinz. Interactions between semiconductor nanowires and living cells. *Journal of Physics: Condensed Matter*, 27(23):233103, 2015.

[76] Valeria Caprettini, Gabriele C. Messina, Michele Dipalo, Rosanna La Rocca, Andrea Cerea, and Francesco De Angelis. SERS spectroscopy, electrical recording and intracellular injection in neuronal networks with 3D plasmonic nanoantennas. 9740:974002, 2016.

[77] Ciro Chiappini, Jonathan O. Martinez, Enrica De Rosa, Carina S. Almeida, Ennio Tasciotti, and Molly M. Stevens. Biodegradable nanoneedles for localized delivery of nanoparticles in vivo: Exploring the biointerface. *ACS Nano*, 9(5):5500–5509, 2015.

[78] Xi Xie, Alexander M Xu, Sergio Leal-Ortiz, Yuhong Cao, Craig C Garner, and Nicholas a Melosh. Nanostraw - Electroporation System for Highly Efficient Intracellular Delivery and Transfection. *ACS Nano*, 7(5):4351–4358, 2013.

[79] Martin W. Hetzer. The nuclear envelope. *Cold Spring Harbor perspectives in biology*, 2(3):1–16, 2010.

[80] Mario Malerba, Alessandro Alabastri, Ermanno Miele, Pierfrancesco Zilio, Maddalena Patrini, Daniele Bajoni, Gabriele C. Messina, Michele Dipalo,

Andrea Toma, Remo Proietti Zaccaria, and Francesco De Angelis. 3D vertical nanostructures for enhanced infrared plasmonics. *Scientific Reports*, 5:16436, nov 2015.

[81] Christoph Krafft, Lars Neudert, Thomas Simat, and Reiner Salzer. Near infrared Raman spectra of human brain lipids. *Spectrochimica Acta - Part A: Molecular and Biomolecular Spectroscopy*, 61(7):1529–1535, 2005.

[82] A. Rygula, K. Majzner, K. M. Marzec, A. Kaczor, M. Pilarczyk, and M. Baranska. Raman spectroscopy of proteins: A review. *Journal of Raman Spectroscopy*, 44(8):1061–1076, 2013.

[83] Matthew D Hodges, Jemma G Kelly, Adam J Bentley, Simon Fogarty, Imran I Patel, Francis L Martin, and Nigel J Fullwood. Combining Immunolabeling and Spectroscopy on Cell Membranes. *ACS nano*, (12):9535–9541, 2011.

[84] Félix Lussier, Thibault Brule, Marie-Josée Bourque, Charles Ducrot, Louis-Éric Trudeau, and Jean-Francois Masson. FDSERS17 Dynamic SERS nanosensor for neurotransmitters sensing near neurons. *Faraday Discuss.*, 2017.

[85] Katrin Kneipp, Abigail S. Haka, Kneipp Harald, Badizadegan Kamran, Noriko Yoshizawa, Charles Boone, Karen E. Shafer-Perltier, Jason T. Motz, Ramachandra R. Dasari, and ;Michael S: Feld. Surface-Enhanced Raman Spectroscopy in Single Living Cells Using Gold Nanoparticles, 2002.

[86] Paul L. McNeil and Richard A. Steinhardt. Loss, restoration, and maintenance of plasma membrane integrity. *Journal of Cell Biology*, 137(1):1–4, 1997.

[87] Christine Salau, Declan J James, and H Chamberlain. Lipid Rafts and the Regulation of Exocytosis. *Traffic*, pages 1–10, 2004.

[88] Changwon Lee, Randy P. Carney, Sidhartha Hazari, Zachary J. Smith, Alisha Knudson, Christopher S. Robertson, Kit S. Lam, and Sebastian Wachsmann-Hogiu. 3D plasmonic nanobowl platform for the study of exosomes in solution. *Nanoscale*, 7(20):9290–9297, 2015.

[89] K. Czamara, K. Majzner, M. Z. Pacia, K. Kochan, Agnieszka Kaczor, and M. Baranska. Raman spectroscopy of lipids: A review. *Journal of Raman Spectroscopy*, 46(1):4–20, 2015.

[90] Zanyar Movasaghi, Shazza Rehman, and Ihtesham U. Rehman. Raman Spectroscopy of Biological Tissues. *Applied Spectroscopy Reviews*, 42(5):493–541, 2007.

[91] Rina K. Dukor. Vibrational Spectroscopy in the Detection of Cancer. *Biomedical Applications*, 5:3335–2259, 2002.

[92] Charalambos Kallepitis, Mads S. Bergholt, Manuel M. Mazo, Vincent Leonardo, Stacey C. Skaalure, Stephanie A. Maynard, and Molly M. Stevens. Quantitative volumetric Raman imaging of three dimensional cell cultures. *Nature Communications*, 8:14843, 2017.

[93] A. J. Ruiz-Chica, M. A. Medina, F. Sánchez-Jiménez, and F. J. Ramírez. Characterization by Raman spectroscopy of conformational changes on guanine–cytosine and adenine–thymine oligonucleotides induced by aminooxy analogues of spermidine. *Journal of Raman Spectroscopy*, 35(2):93–100, 2004.

[94] G Shetty, C Kendall, N Shepherd, N Stone, and H Barr. Raman spectroscopy: elucidation of biochemical changes in carcinogenesis of oesophagus. *British Journal of Cancer*, 94(10):1460–1464, 2006.

[95] Jean Gruenberg and F Gisou van der Goot. Mechanisms of pathogen entry through the endosomal compartments. *Nature reviews. Molecular cell biology*, 7(7):495–504, jul 2006.

[96] Ian H Stevenson and Konrad P Kording. How advances in neural recording affect data analysis. *Nature neuroscience*, 14:139–142, 2011.